Identifying a Universal Activity Descriptor and a Unifying Mechanism Concept on Perovskite Oxides for Green Hydrogen Production

Daqin Guan,* Hengyue Xu, Qingwen Zhang, Yu-Cheng Huang, Chenliang Shi, Yu-Chung Chang, Xiaomin Xu, Jiayi Tang, Yuxing Gu, Chih-Wen Pao, Shu-Chih Haw, Jin-Ming Chen, Zhiwei Hu,* Meng Ni,* and Zongping Shao*

Producing indispensable hydrogen and oxygen for social development via water electrolysis shows more prospects than other technologies. Although electrocatalysts have been explored for centuries, a universal activity descriptor for both hydrogen-evolution reaction (HER) and oxygen-evolution reaction (OER) is not yet developed. Moreover, a unifying concept is not yet established to simultaneously understand HER/OER mechanisms. Here, the relationships between HER/OER activities in three common electrolytes and over ten representative material properties on 12 3d-metal-based model oxides are rationally bridged through statistical methodologies. The orbital charge-transfer energy (Δ) can serve as an ideal universal descriptor, where a neither too large nor too small Δ ($\approx$1 eV) with optimal electron-cloud density around Fermi level affords the best activities, fulfilling Sabatier's principle. Systematic experiments and computations unravel that pristine oxide with $\Delta \approx 1$ eV possesses metal-like high-valence configurations and active lattice-oxygen sites to help adsorb key protons in HER and induce lattice-oxygen participation in the OER, respectively. After reactions, partially generated metals in the HER and high-valence hydroxides in the OER dominate proton adsorption and couple with pristine lattice-oxygen activation, respectively. These can be successfully rationalized by the unifying orbital charge-transfer theory. This work provides the foundation of rational material design and mechanism understanding for many potential applications.

1. Introduction

Hydrogen and oxygen play vital roles in current life, production, medicine, aerospace, and the net-zero plan.[1,2] Besides indispensable oxygen, the International Energy Agency and Hydrogen Council predict that global hydrogen demand will exceed 500 Mt[3] and create $\approx$USD 3 trillion revenues via hydrogen-value chains in 2050.[4] Efficient production of hydrogen and oxygen thus becomes one of the important cornerstones for sustainable development. Owing to the high maturity and low cost (only $\approx$1–2 USD kg^{-1} H$_2$), $\approx$95% of current hydrogen is produced from the reforming or gasification of nonrenewable fossil fuels,[5] namely the traditional "grey hydrogen" mode. However, impure "grey hydrogen" requires further complex purification for use, and 1 kg produced "grey hydrogen" generates $\approx$10 kg CO$_2$ emissions.[6] Oxygen is usually produced via the separation of liquid air. Although this technology shows advantages of high oxygen output and abundant air resources, complicated large facilities for cooling, purification, compression, and distillation are required.[7] Moreover, the above two technologies can only produce hydrogen or

D. Guan, X. Xu, J. Tang, Z. Shao
WA School of Mines: Minerals
Energy, and Chemical Engineering
Curtin University
Perth, Western Australia 6845, Australia
E-mail: daqin.guan@polyu.edu.hk; zongping.shao@curtin.edu.au

D. Guan, M. Ni
Department of Building and Real Estate
Research Institute for Sustainable Urban Development (RISUD) and Research Institute for Smart Energy (RISE)
The Hong Kong Polytechnic University
Hung Hom, Kowloon, Hong Kong 999077, China
E-mail: meng.ni@polyu.edu.hk

H. Xu
Institute of Biopharmaceutical and Health Engineering
Tsinghua Shenzhen International Graduate School
Tsinghua University
Shenzhen 518055, China

Q. Zhang
Department of Building and Real Estate
The Hong Kong Polytechnic University
Hung Hom, Kowloon, Hong Kong 999077, China

oxygen. Utilizing electricity transformed from renewable solar, wind, and hydro power as input, water electrolysis can simultaneously produce high-purity hydrogen and oxygen with the merits of abundant resources, simple processes, zero-carbon emissions, and environmental friendliness,[8] which is also called "green hydrogen" production. Due to the above features, "green hydrogen" is estimated to replace ≈30% of "grey hydrogen" in 2030;[4] whereas, the current production cost of "green hydrogen" is still ≈4–5 times that of "grey hydrogen,"[5] where electricity consumes the major cost.[8] As an important way to lower the cost, effectively screening and developing efficient electrocatalysts for hydrogen-evolving reaction (HER) and oxygen-evolving reaction (OER) have been the main focus during the past hundred years of fundamental research and commercialization.[9]

Material activity descriptors establish the relationships between catalyst physicochemical properties and their performance, which can effectively save time and cost to facilitate the design and development of efficient electrocatalysts for "green hydrogen" production. During the past decades, numerous experimental and computational activity descriptors have been successfully explored. For OER activity descriptors, adsorption strength of oxygen species,[10] orbital e_g occupancy,[11] O 2p band center,[12] charge-transfer energy (Δ),[13] outer electrons,[14] coordination number,[15] bond strength,[16] formation energy,[17] enthalpy,[18] Curie/Néel temperature,[19] electrochemical redox potential,[20] and electrochemical-step symmetry index[21] have been developed. In terms of HER activity descriptors, proton adsorption strength,[22] d band center,[23] valence state,[24] ionic electronegativity,[25] strain,[26] and tolerance factor[27] have been reported. Although great advancements have been made, a universal activity descriptor for both HER and OER in different electrolytes has not yet been extracted from the material multiple features (**Figure 1**a). Further, scientific and precise analysis tools are still lacking to rationally evaluate the property–activity relationships and the independence and controllability of potential descriptors. Once such universal activity descriptors with fine independence and controllability are found, considerable time and cost from trials and errors in electrocatalyst development will be saved for basic research and commercialization, which still remains an extremely challenging but meaningful scientific issue.

The successful establishment of universal activity descriptors will promote the effective screening and design of material pristine states, while insights into the catalysis mechanisms before and after reactions are also important to understand the underlying roles of activity descriptors. After decades of efforts, the HER/OER mechanisms have been well established[28,29] and the

focus has shifted from the initial catalysis mechanisms to activated catalysis processes.[30] For example, electrocatalysts may be partially reduced into metals after HER[31,32] and oxidized into hydroxides after OER[31,33] (Figure 1b). Actually, the activated catalysis processes strongly rely on material initial states, where the different properties of pristine material can reach to different active sites and catalysis mechanisms after reactions[34] (Figure 1b). Therefore, mechanism investigations based on properties of pristine material and activated states are both critical. However, to date, a unifying theory has not been found or established to simultaneously and rationally describe the HER/OER mechanisms before and after reactions. If successful, such a unifying theory will serve as the powerful mechanism analysis tool and foundation.

To solve the above two important issues, we choose 12 3d transition-metal-based (Mn, Fe, Co, Ni) perovskite oxides with high physicochemical property degrees of freedom[35] as the model system (Figure 1a), namely ABO_{3-x} (A = La and Sr, B = pure Mn, Fe, Co, or Ni). Utilizing the powerful significance analysis and regression analysis, we precisely evaluate the correlations between the HER/OER performance in three common electrolytes (1 M KOH, 1 M KPi, and 6 M KOH) and 13 representative catalyst properties (macroscopic physiochemical, molecular-level structural, and electronic structural features) on the model oxides for the first time. The independence and controllability of potential descriptors are further compared by the correlation analysis, ultimately identifying the main and secondary universal activity descriptors. Specifically, orbital Δ determined by both metal 3d and O 2p orbitals can be the main ideal universal descriptor. When material Δ is too negative, the mixing of occupied and unoccupied metal 3d–O 2p orbitals at Fermi level (E_F) is excessive, leading to unstable O 2p holes and inferior activities. As material Δ is too large, the electron cloud density of occupied and unoccupied metal 3d–O 2p orbitals around E_F is low, resulting in few active orbitals and poor activities as well. With a neither too large nor too small Δ (≈1 eV), such oxides exhibit the optimum catalytic activities, following the Sabatier's principle. Further systematic mechanism experiments, spectral characterizations, and first-principle calculations reveal that the metal-like (refer to small bandgap here) high-valence configurations and relatively high electron cloud density of O 2p orbitals around E_F on pristine oxide with Δ ≈ 1 eV can enhance the key proton-adsorption steps in HER and the lattice-oxygen participation in OER, respectively. After reductive HER and oxidative OER, initial metal-like sites are replaced by partially formed metals to further optimize the proton adsorption, while the generated high-valence hydroxides couple with pristine lattice-oxygen activation. Noteworthily, the orbital charge-transfer theory can well demonstrate all these findings, endowing it as the unifying mechanism analysis tool and foundation. Under near-industrial conditions, the obtained oxide with Δ ≈ 1 eV even shows a much superior price activity than the state-of-the-art noble-metal benchmarks in the anion exchange membrane electrolyzer (AEME). To the best of our knowledge, this is the first time to successfully identify a universal activity descriptor and a unifying mechanism concept for "green hydrogen" production, which will pave the way for rational material design and mechanism insights in many potential fields.

Y.-C. Huang, Y.-C. Chang, C.-W. Pao, S.-C. Haw, J.-M. Chen
National Synchrotron Radiation Research Center
101 Hsin-Ann Road, Hsinchu 30076, Taiwan
C. Shi, Y. Gu, Z. Shao
State Key Laboratory of Materials-Oriented Chemical Engineering
College of Chemical Engineering
Nanjing Tech University
Nanjing 211800, China
Z. Hu
Max-Planck-Institute for Chemical Physics of Solids
Nöthnitzer Str. 40, 01187 Dresden, Germany
E-mail: zhiwei.hu@cpfs.mpg.de
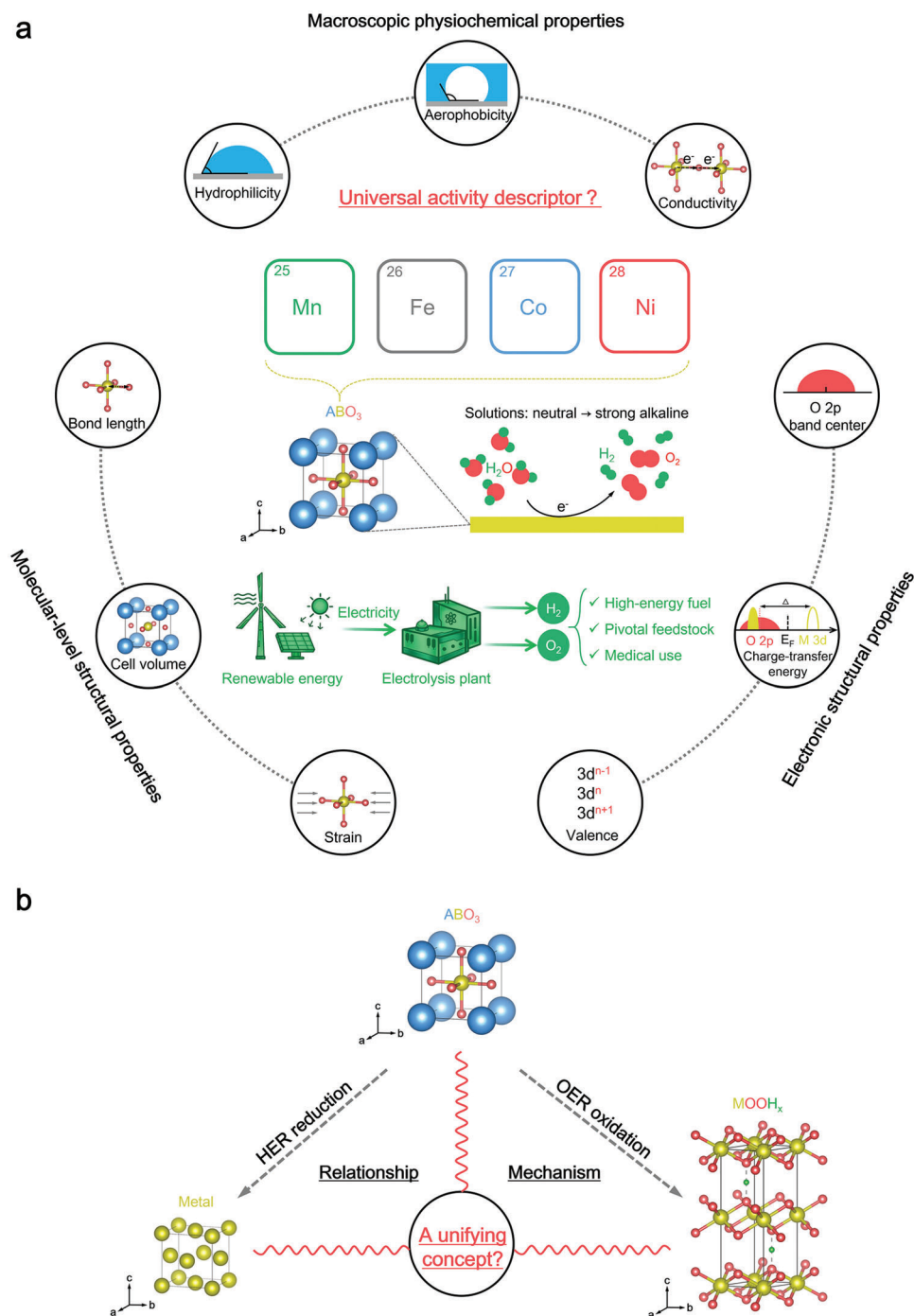
Figure 1. a,b) Schematic diagrams: a) identifying a universal activity descriptor from various material macroscopic physiochemical, molecular-level structural, and electronic structural properties and b) for finding a unifying mechanism concept for HER/OER before and after reactions on 3d transition-metal-based (Mn, Fe, Co, and Ni) perovskite oxides in multiple electrolytes for "green hydrogen" production.

2. Results and Discussion

With flexible element choice, abundant physicochemical properties, and facile synthesis processes, perovskite oxides (ABO_3, A = alkaline-earth/rare-earth cations and B = transition-metal ions) have been pushed to the forefront of "green hydrogen" production during the past decades[35,36] (Figure 1a). To iden-

tify a universal activity descriptor from materials' numerous features, we selected perovskite oxide as the model system. As shown in Figure 1a, the studied representative physicochemical properties in our work can be divided into three categories, including macroscopic physiochemical properties (i.e., hydrophilicity, aerophobicity, and conductivity), molecular-level structural properties (i.e., bond length, cell volume, and

strain), and electronic structural properties (i.e., valence state, charge-transfer energy, O 2p band center, and orbital bandgap). Considering that cost-effective 3d transition-metal-based catalysts are promising to replace precious-metal-based benchmarks in non-acidic water electrolysis,[28] we synthesized 12 $La_ySr_{1-y}MO_{3-x}$ (M = pure Mn, Fe, Co or Ni; y = 1, 0.75, and 0.5) perovskite oxides via the traditional sol–gel method for HER/OER investigations in 1 м KOH, 1 м KPi, and 6 м KOH (Figure 1a). The property–activity relationships and the independence and controllability of potential universal descriptors will be rationally demonstrated by the powerful statistical analysis. Further, to find or establish a unifying mechanism concept for HER/OER before and after reactions (Figure 1b), systematic mechanism experiments, spectral characterizations, and density functional theory (DFT) calculations will be conducted.

2.1. Macroscopic Physiochemical Properties

Material macroscopic physiochemical features such as hydrophilicity, aerophobicity, and conductivity may exert some roles in water electrolysis. Therefore, we first studied the correlations between material macroscopic physiochemical properties and their HER/OER performance in widely used 1 м KOH. To exclude the effects of material surface areas and correlate well with the literatures,[11,12,25] we compared the intrinsic HER/OER activities normalized to the surface areas of model oxides, which were measured by the Brunauer–Emmett–Teller (BET) method (Tables S1–S3, Supporting Information). According to the reported comparison criterion[11,12] and the intrinsic HER/OER current densities of our model oxides, we chose the OER overpotentials at 200 μA cm$^{-2}_{oxide}$ and the HER overpotentials at −200 μA cm$^{-2}_{oxide}$ for comparison. In addition, to rationally and precisely analyze the property–activity relationships, we applied the methodologies of significance analysis[37] and regression analysis,[38] where the degree of correlation between properties and activities could be quantified by the obtained p value. If the p value was ≤ 0.05, the property–activity relationship was significant; when the p value was between 0.05 and 0.1, the correlation was slightly significant; and if the p value was >0.1, the relevance was insignificant. When the analyzed property–activity relationship was significant (p value ≤ 0.05), we could utilize regression analysis to further obtain the detailed relation equation.

We obtained the solid–liquid contact angle by dropping the liquid on the electrode films (Figure S1, Supporting Information). When the solid–liquid contact angle was smaller than 90°, the catalyst surface showed hydrophilicity, while it was larger than 90° for the hydrophobic surface (**Figure 2**a).[39] The solid–liquid contact angles of our model oxides were all larger than 90°, implying their hydrophobic features (Figure S1 and Table S4, Supporting Information). After analyzing the significance between solid–liquid contact angle and intrinsic HER/OER activities (Figure 2b,c; Table S5, Supporting Information), we found that the relationship between solid–liquid contact angle and intrinsic HER activities was slightly significant (p value < 0.1), while that for intrinsic OER activities was not significant (p value > 0.1). This means material solid–liquid contact angle cannot serve as the universal activity descriptor.

By extracting the solid–gas (H$_2$ or O$_2$) contact angle from the electrode films that react during HER or OER (Figures S2 and S3 and Table S4, Supporting Information), we can compare the aerophobicity of the model system, where aerophobicity exhibits a solid–gas contact angle of >90° while aerophilicity shows a solid–gas contact angle of <90° (Figure 2d).[39] As displayed in Figures S2 and S3 and Table S4, Supporting Information, the model oxides all show aerophobicity to H$_2$ and aerophilicity to O$_2$. Noteworthily, the relationships between solid–H$_2$/O$_2$ contact angles (x) and intrinsic HER/OER activities (y) are both significant with p values of <0.05 (Figure 2e,f; Table S5, Supporting Information). Through further regression analysis, the detailed relation equations of $y = −12.029x + 1580.587$ and $y = −5.572x + 775.900$ are obtained for the solid–H$_2$ contact angle vs intrinsic HER activities and the solid–O$_2$ contact angle vs intrinsic OER activities, respectively. This indicates that with an enlarged solid–gas contact angle (namely enhanced aerophobicity), the HER and OER activities both improve accordingly, which can be attributed to the timely releasing of gas products without covering material active surfaces. Therefore, material solid–gas contact angle can be a potential universal activity descriptor. Evaluations of the independence and controllability of potential universal activity descriptors will be further discussed below.

For material conductivity (Figure 2g), we first measured material electrical conductivity by using a four-probe method. We then found that the relationships between this parameter and intrinsic HER/OER activities were not significant with p values of >0.1 (Figure S4, Tables S4 and S5, Supporting Information). It is worth noting that for the same 3d-metal-based oxides, the activities are enhanced with improved material electrical conductivity. To further compare the electron transport during HER and OER, we measured the electrochemical impedance spectroscopy (EIS) for the model system, where the polarization resistance (R_p) was widely used to reflect the catalysis resistance[40,41] (Table S4, Supporting Information). Similarly, for oxides with the same 3d metal, the activities were also improved with decreasing R_p values (Figure 2h,i). Statistical analysis shows that the relationship between HER R_p (x) and intrinsic HER activity (y) is significant (p value < 0.05) with a regression equation of $y = 0.852x + 301.349$, while that for OER is not significant with a p value of >0.1 (Figure 2h,i; Table S5, Supporting Information). These findings exclude the possibilities of both material electrical conductivity and electron transport during reactions as the universal activity descriptors. However, for oxides with the same 3d element, two parameters can be applied for semiempirical comparisons.

2.2. Molecular-Level Structural Properties

As the next step, we studied the correlations between material molecular-level structural features (i.e., bond length, cell volume, and strain) and intrinsic HER/OER activities. To acquire the information of average 3d−O bond length and structural cell volume, we performed the structural refinement for the X-ray diffraction (XRD) patterns of all the samples (Figure
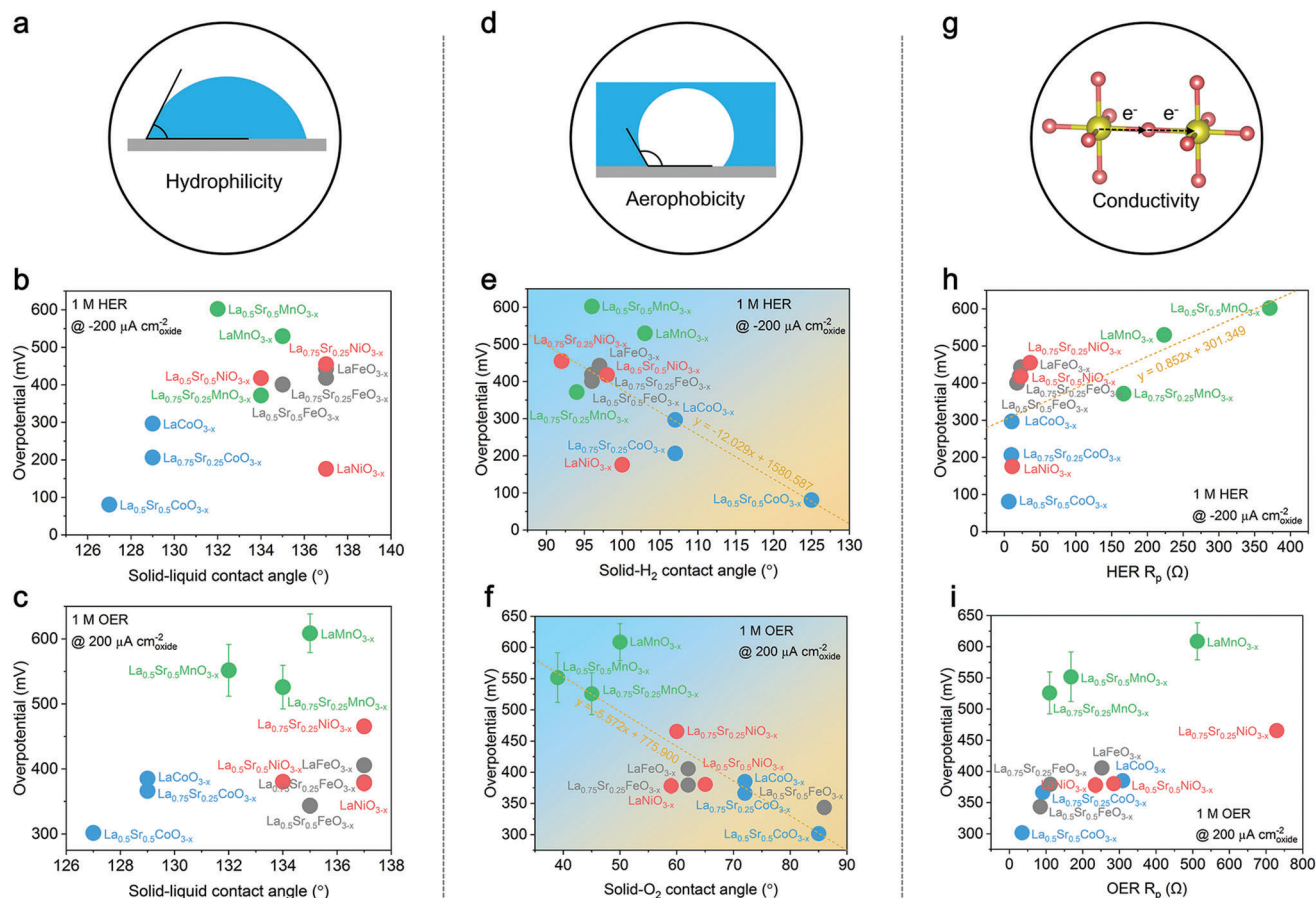
Figure 2. Relationships between material macroscopic physiochemical properties and intrinsic HER/OER activities using linear regression (sample size $n = 12$). a–c) Correlations between solid–liquid contact angle and intrinsic HER/OER activities (p value < 0.1 for HER and p value > 0.1 for OER). d–f) Relevance between solid–gas contact angle and intrinsic HER/OER activities (p values < 0.05). g–i) Relationships between conductivity and intrinsic HER/OER activities (p value < 0.05 for HER and p value > 0.1 for OER). The p-values are calculated using one-way ANOVA.

S5 and Table S6, Supporting Information). The fine XRD refinement results can provide details on average 3d–O bond length and structural cell volume (Table S7, Supporting Information). As illustrated in Table S5, Supporting Information; **Figure 3**a–f, significance analysis shows that only the relationship between bond length and intrinsic HER activity is slightly significant (p value < 0.1); the other correlations are not significant (p values > 0.1). To acquire the strain component (Figure 3g), Williamson–Hall analysis was conducted on the XRD patterns of the model system. Williamson–Hall analysis follows the equation of $4\epsilon\sin\theta = \beta\cos\theta - k\lambda/D$ to determine the strain component (ϵ), where k is constant (0.94) and θ, β, λ, and D represent the diffraction degree, peak width at half-maximum intensity, wavelength, and particle size, respectively.[42,43] Through the slope values from the curves of $\beta\cos\theta$ vs $4\sin\theta$, the strain component ϵ can be obtained (Table S7, Supporting Information). Subsequent significance analysis reveals that both the relationships between the strain component and intrinsic HER/OER activities are not significant with p values of >0.1 (Table S5, Supporting Information; Figure 3h,i). The above findings imply that structural bond length, cell vol-

ume, and strain are all unable to be the universal activity descriptors.

2.3. Electronic Structural Properties

Then, we investigated the underlying relationships between material electronic structural properties and their intrinsic HER/OER activities. Representative material electronic structural features such as 3d metal valence state, orbital charge-transfer energy, O 2p band center, and bandgap are generally used to demonstrate material activity origins, where we further evaluate their potentials to become the universal activity descriptors.

The valence state of 3d metal elements (**Figure 4**a) plays an important role in the reductive and oxidative reactions. To accurately acquire material valence state, the X-ray absorption near-edge structure (XANES) spectra at the 3d-K edges are usually applied for analysis.[44–47] The energy positions at normalized absorption of ≈0.7–0.8 on 3d-K XANES spectra are widely used to determine the 3d metal valence states.[44–47] Specifically, a shift of

**ADVANCED
SCIENCE NEWS**

www.advancedsciencenews.com
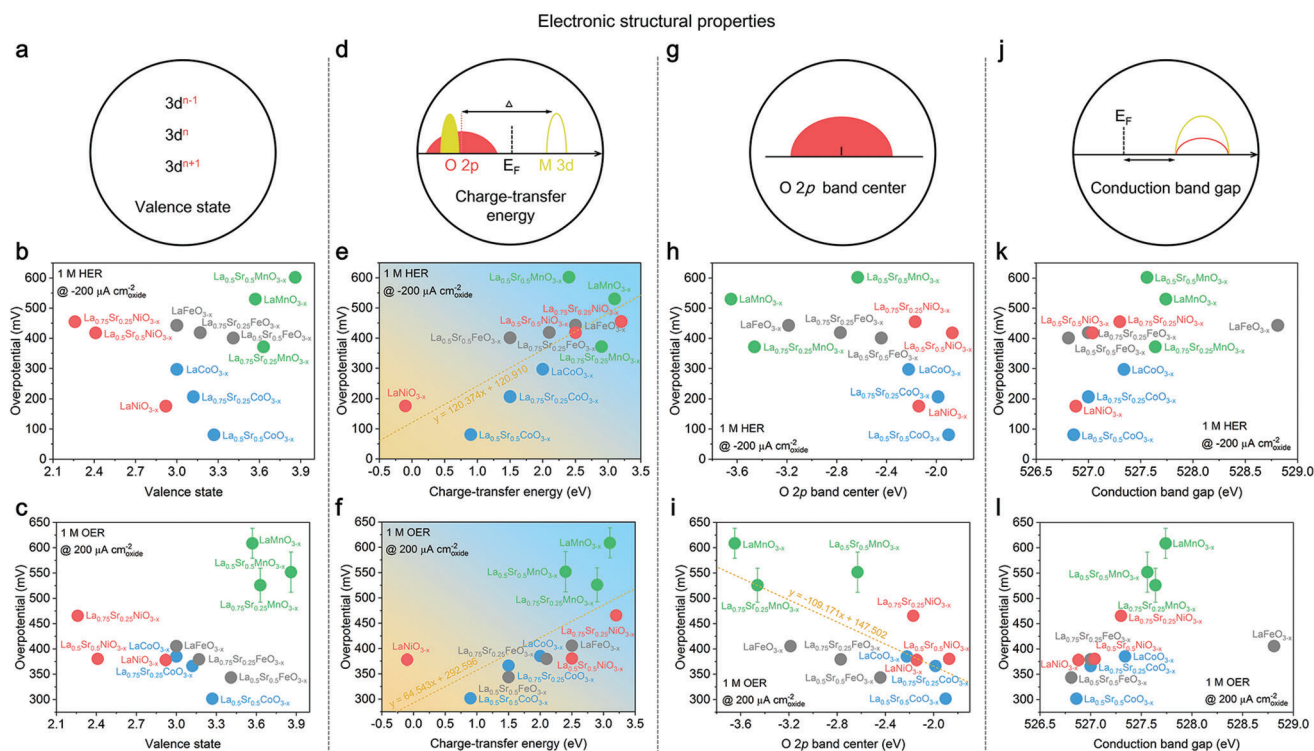
**ADVANCED
MATERIALS**

www.advmat.de
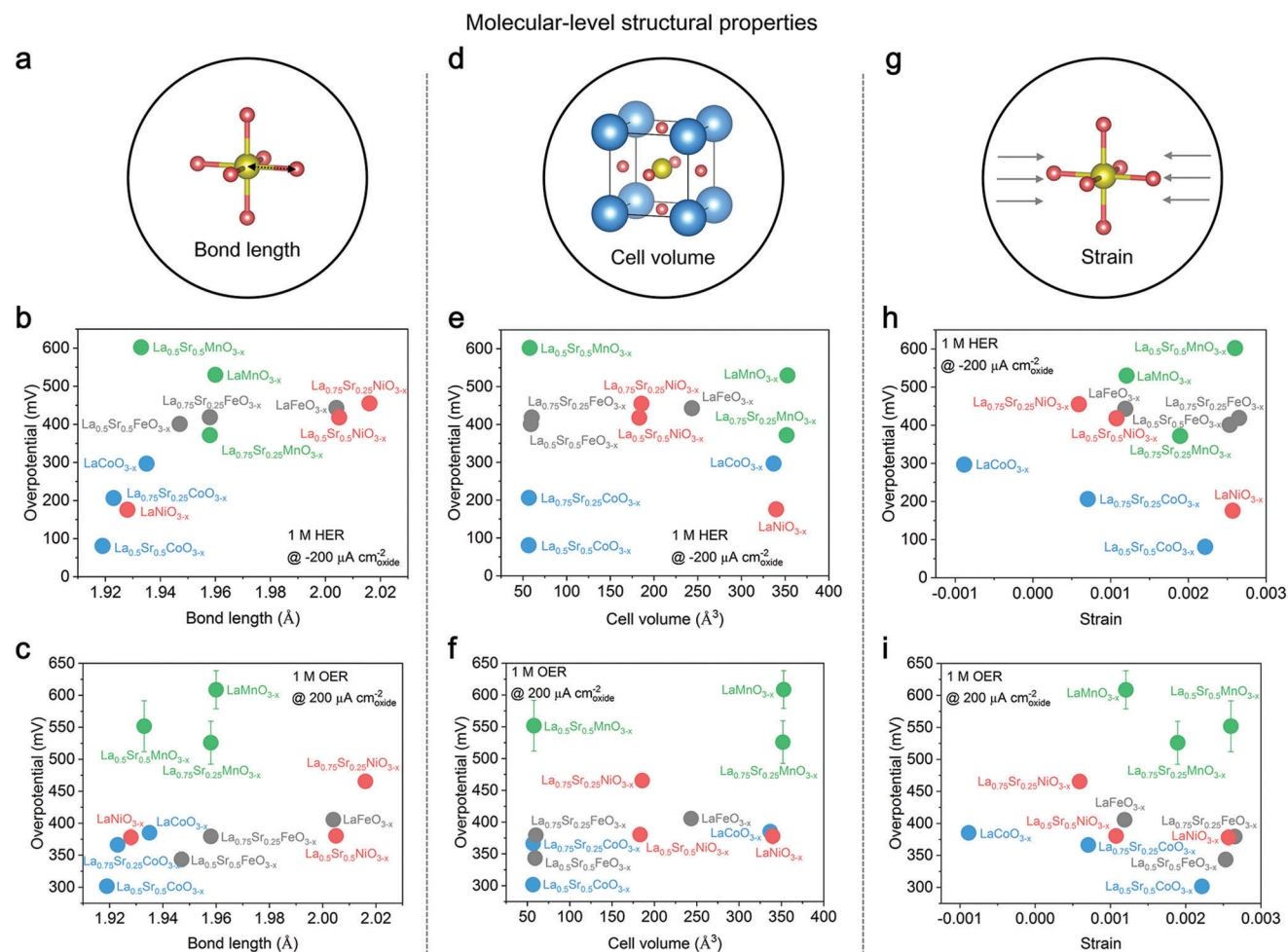
Figure 3. Relationships between material molecular-level structural properties and intrinsic HER/OER activities using linear regression (sample size n = 12). a–c) Correlations between bond length and intrinsic HER/OER activities (p value < 0.1 for HER and p value > 0.1 for OER). d–f) Relevance between cell volume and intrinsic HER/OER activities (p values > 0.1). g–i) Relationships between strain and intrinsic HER/OER activities (p values > 0.1). The p-values are calculated using one-way ANOVA.

the energy position at normalized absorption of ≈0.7–0.8 on 3d-K XANES spectra to the higher energies indicates an increase in the 3d metal valence, where the detailed valence state can be identified by linear interpolation with the standards.[44–47] The physical origin of this method lies in that the energy position of the white line is strongly affected by material crystal structure (not valence-sensitive region) during the 1s→4p transition, while the energy positions at the low normalized absorptions of <0.7 are greatly dominated by the intersite screening effects and quadrupole transition (also not valence-sensitive regions).[48] Therefore, the normalized absorption of ≈0.7–0.8 on 3d-K XANES spectra is rationally chosen for the valence analysis.[44–48]

Moreover, to experimentally demonstrate the plausibility of this method, we measured the Co-K XANES spectra of various single crystals with pure Co^{2+}, Co^{3+}, or Co^{4+} states.[44,47] Their Co-K XANES spectra revealed that the energy positions at normalized absorption of ≈0.7–0.8 for the standards with the same Co valence were consistent, while those at normalized absorption below 0.7 for the standards with the same Co valence were different (Figure S6, Supporting Information), which

means the inter-site screening effects and quadrupole transition (not valence state) dominate at normalized absorptions of <0.7. Here, the detailed valence states of our model system were obtained via the linear interpolation with the standards (Figures S7–S10 and Table S8, Supporting Information) in line with many literatures.[44–48] Material surface valence state could be analyzed by 3d-L X-ray absorption spectroscopy (XAS) measured in the surface-sensitive total electron yield (TEY) mode, where the center of spectral weight of the L-edge peak moves to higher energy positions with the increasing 3d metal valence state[44,49–51] (see standards in Figures S11–S14, Supporting Information). By combining the 3d-L XAS spectra of standards, we verified the consistent tendency of valence information on the model system extracted from 3d-L XAS and 3d-K XANES spectra (Figures S11–S14, Supporting Information). As presented in Table S5, Supporting Information; Figure 4b,c, the relationships between valence state and intrinsic HER/OER activities are not significant (p values > 0.1), ruling out the potential of material valence to become the universal activity descriptor.

Figure 4. Relationships between material electronic structural properties and intrinsic HER/OER activities using linear regression (sample size $n = 12$). a–c) Correlations between valence state and intrinsic HER/OER activities (p values > 0.1). d–f) Relevance between charge-transfer energy and intrinsic HER/OER activities (p values < 0.05). g–i) Relationships between the O 2p band center and intrinsic HER/OER activities (p value < 0.1 for HER and p value < 0.05 for OER). j–l) Correlations between the conduction bandgap and intrinsic HER/OER activities (p values > 0.1). The p-values are calculated using one-way ANOVA.

Charge-transfer energy Δ is defined as the energy difference between the orbital centers of O 2p orbital and unoccupied metal 3d orbital[52,53] (Figure 4d). This parameter simultaneously associates with the occupied and unoccupied non-metal and metal orbitals, which was assigned to the OER descriptor.[13] According to the previous studies in physics,[52,53] for the same 3d-metal-based oxides (namely the same Fe- or Mn- or Co- or Ni-based materials), the correlation between Δ value and 3d metal valence follows a linear relation, namely, the Δ value reduces with the increasing 3d metal valence. For different 3d elements with the same valence state, the Δ value reduces from Mn^{n+} to Fe^{n+}, Co^{n+}, and further to Ni^{n+}.[52,53] Thus, we can achieve the charge-transfer energy of the model system through this linear relationship using standards[47,52,53] (Figures S15–S18, Table S8, Supporting Information; Figure 4e,f). As expected, significance analysis verifies that the correlation between material Δ (x) and intrinsic OER activity (y) is significant (p value < 0.05) in line with the literatures,[13,54] where the relation equation is $y = 64.543x + 292.596$ (Table S5, Supporting Information; Figure 4f). Noteworthily, the relationship between material Δ (x) and intrinsic HER activity (y) is also significant (p value < 0.05) with a regression equation of $y = 120.374x + 120.910$ (Table S5, Supporting Information; Figure 4e). These findings indicate that charge-transfer energy Δ can be reasonably used as a potential universal activity descriptor. The phenomenon of the improved catalytic activities of materials with the decreasing Δ values can be ascribed to the shortened orbital bandgap, more active orbitals, and higher

electron cloud density around E_F (all induced by the reducing Δ values). These will endow the material with metal-like configurations and relatively active lattice-oxygen sites to boost the HER and OER, respectively, which will be further illustrated below.

For 3d-metal-based oxides, the O 2p band center (Figure 4g) extracted from orbital calculations has also been applied as the OER activity descriptor.[12] Based on the structural information from the XRD analysis, we also performed the calculations of the orbital density of states (DOS) to obtain the O 2p band center for our model oxides (Table S8, Supporting Information; Figure 4h,i). In agreement with prior findings,[12] our significance analysis also proves that the relationship between material O 2p band center (x) and intrinsic OER activity (y) is significant (p value < 0.05, relation equation: $y = -109.171x + 147.502$), as revealed in Table S5, Supporting Information; Figure 4i. However, for HER, it is only slightly significant with a p value of <0.1 (Table S5, Supporting Information; Figure 4h). Therefore, material O 2p band center is not an ideal potential universal activity descriptor, especially for neutral HER and OER (p values > 0.1 as discussed below).

Orbital bandgap is one of the important properties for semiconductor oxides, where both material electron transitions and electron flows triggered by adsorbed species need to cross material unoccupied orbital bandgap (i.e., conduction bandgap) for occupation (Figure 4j). In physics, it is well known that the bandgap reduces with the increase in valence state of the 3d-metal-based oxides, leading to the transition from strong insulator to semiconductor and further to metal-like state.[25] It has been reported

2305074 (7 of 17)

that the conduction bandgap can be acquired from the experimental O-*K* XAS spectra.[47,55] We identified material conduction bandgap by the tangents on the pre-edge peaks in the O-*K* XAS spectra (Figures S19–S22 and Table S8, Supporting Information; Figure 4k,l). Our significance analysis implies that the relationships between material conduction bandgap and intrinsic HER/OER activities are not significant (Table S5, Supporting Information; Figure 4k,l), which cannot be the potential universal activity descriptor as well.

2.4. The Main and Secondary Universal Activity Descriptors

The above statistical analysis under the linear function unravels that material solid–gas contact angle and orbital charge-transfer energy can be the potential universal activity descriptors. To further verify this, we also utilized the quadratic function and exponential function to establish the possible relationships. By combining the new results under the quadratic/exponential functions (Table S9, Supporting Information) with the relationships under the linear function (Table S5, Supporting Information), we can still conclude that only solid–gas contact angle and orbital charge-transfer energy can be the potential universal activity descriptors for both HER and OER performance with *p* values of <0.05. Here, we propose three fundamental requirements for a parameter to become an ideal or near-ideal universal activity descriptor: i) effective relevance with both HER and OER performance; ii) high independence for facile modulation and control; and iii) available efficient strategies to master or predict the parameter. For condition (i), both material solid–gas contact angle and orbital charge-transfer energy can meet this requirement. The condition (ii) is proposed to maximally lower the complexity of parameter modulation without suffering from many other factors. The condition (iii) is also necessary because we need to clearly understand how to design and control the parameter via the existing strategies prior to experiments or calculations, which will help save considerable time and cost for material screening and design.

To compare the independence of the material solid–gas contact angle and orbital charge-transfer energy, we conducted correlation analysis[56] to study their relationships with other parameters. Similarly, correlation analysis first requires the significance analysis between two parameters, where the significance judgment is the same as discussed above. When the relationship between two parameters is significant (*p* value of <0.05), then the magnitude of the Pearson correlation coefficient can be used to evaluate the degree of correlation between the two parameters.[56] Specifically, the Pearson correlation coefficient for a parameter versus itself is 1.[56] With enhanced negative or positive correlation between two parameters, the Pearson correlation coefficient is accordingly more negative or positive, respectively.[56] As demonstrated in Table S10, Supporting Information, and **Figure 5**a (red circles), from the perspective of statistics, material solid–H_2 contact angle shows a negative correlation with material solid–liquid contact angle (Pearson correlation coefficient = −0.795), while both R_p of HER and O 2p band center are negatively and positively correlated to material solid–O_2 contact angle with Pearson correlation coefficients of −0.779 and 0.587, respectively. These imply that material solid–gas (H_2 or O_2) contact angle is associated with three other ma-

terial properties from the standpoint of statistics. Notably, material charge-transfer energy only exhibits a relatively weak positive correlation with material bond length (Pearson correlation coefficient = 0.662). Figure 5b displays the detailed graphic relationships between two parameters, namely the corresponding scattering matrix[56] for Figure 5a. Therefore, from the viewpoint of statistics, material charge-transfer energy shows a relatively higher independence to become the optimum universal activity descriptor as compared with material solid–gas (H_2 or O_2) contact angle, fulfilling condition (ii).

In terms of the predictability, material solid–gas contact angle can only be obtained after measuring the synthesized catalysts in reactions, where complex morphology tuning strategies may be applied to control this property.[39] Owing to the linear relation with 3d metal valence,[52,53] the magnitude of charge-transfer energy for catalysts with the same 3d element can be well regulated via facile electron/hole doping, vacancy introduction, and chemical oxidation/reduction methods, fulfilling condition (iii). Therefore, material orbital charge-transfer energy and solid-gas contact angle can serve as the main and secondary universal activity descriptors, respectively.

To analyze the multiple effects of both orbital charge-transfer energy and solid–gas contact angle on activity, we further carried out the significance analysis among the two activity descriptors as well as intrinsic HER/OER activities. The results reveal that the above three follow the significant binary linear relations with *p* values of <0.05 (Table S5, Supporting Information). In detail, the obtained binary linear equations for solid-H_2 contact angle (*x*) vs charge-transfer energy (*y*) vs intrinsic HER activity (*z*) and solid-O_2 contact angle (*x*) vs charge-transfer energy (*y*) vs intrinsic OER activity (*z*) are $z = −7.546x + 86.694y + 951.156$ and $z = −4.543x + 31.171y + 647.308$, respectively (Table S5, Supporting Information; Figure 5c,d). We can observe the negative and positive correlations for solid–gas contact angle vs intrinsic activities and charge-transfer energy vs intrinsic activities, respectively. The multiple-effect relationships are helpful for future rational material design from multi dimensions. To verify the universality of the main universal activity descriptor, we further investigated the relevance between material properties and intrinsic HER/OER activities in 1 M KPi and 6 M KOH. The findings from statistical analysis confirm the high universality and reliability of orbital charge-transfer energy as the ideal universal activity descriptor (Figures S23–S38 and Tables S11 and S12, Supporting Information).

As the next step, we demonstrate the effect origins of the main and secondary universal activity descriptors on performance. As presented on the top of Figure 5e, unoccupied (i.e., conduction band) and occupied (i.e., valence band) orbitals locate above and below the E_F, respectively. When material orbital charge-transfer energy decreases, both the conduction band and the valence band shift toward E_F,[40,47,57] inducing reduced bandgap, more active orbitals, and higher orbital electron cloud density around E_F (Figure 5e). These will endow the material with metal-like clusters and active lattice-oxygen sites to promote HER and OER processes (detailed in the mechanism discussions below). For material solid–gas contact angle, the larger angle indicates the enhanced aerophobicity, which can help timely release H_2/O_2 products and avoid covering active catalysis surfaces for improved performance (Figure 5e bottom).

**ADVANCED
SCIENCE NEWS**

www.advancedsciencenews.com

**ADVANCED
MATERIALS**

www.advmat.de
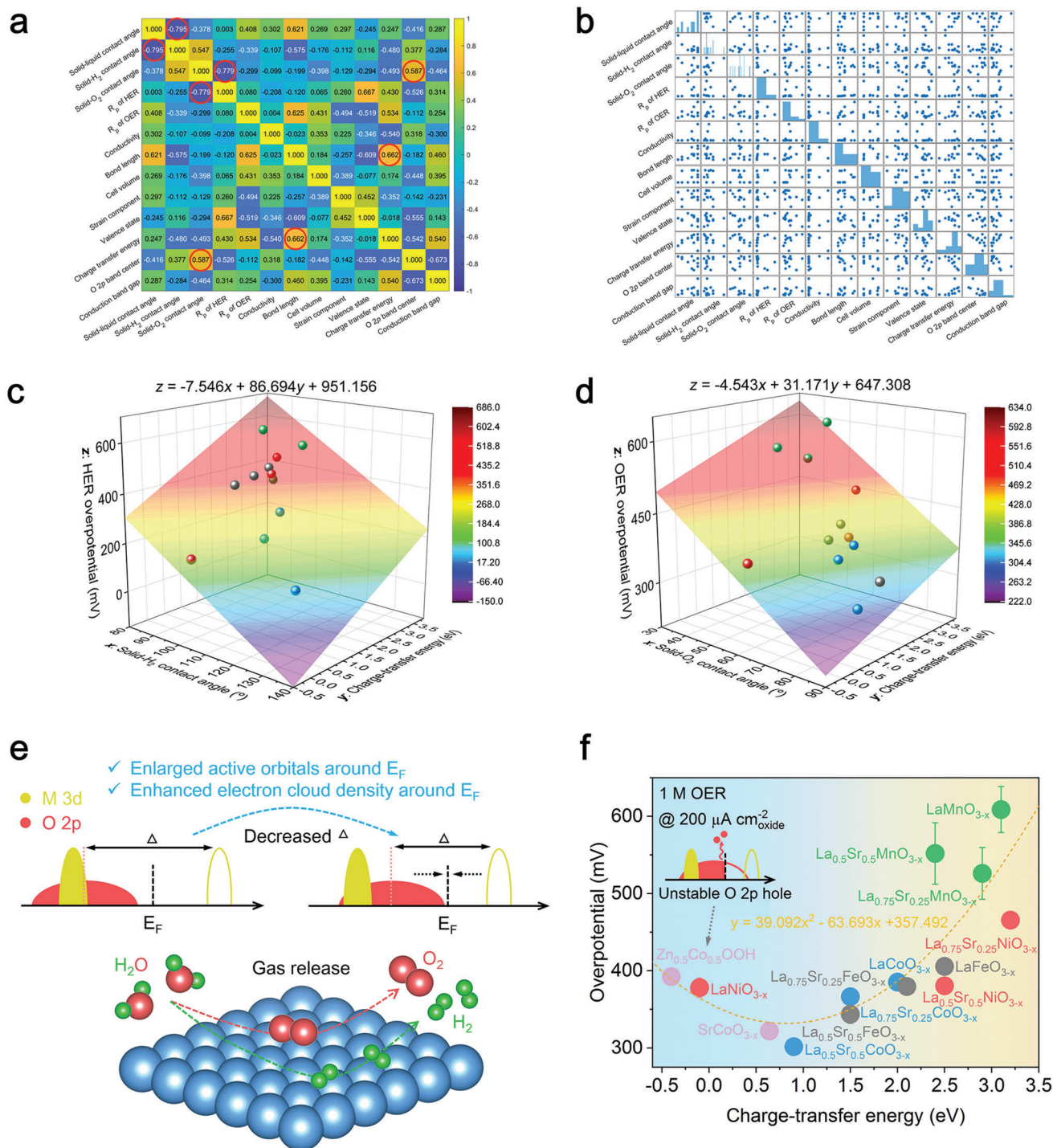
Figure 5. The main and secondary universal activity descriptors. a) Correlation analysis of material properties and b) the corresponding scattering matrix. c) Binary linear relations for solid-H_2 contact angle (x) vs charge-transfer energy (y) vs intrinsic HER activity (z) and d) solid-O_2 contact angle (x) vs charge-transfer energy (y) vs intrinsic OER activity (z). The p-values are calculated using two-way ANOVA (sample size $n = 12$, p values < 0.05). e) Schematic illustrations for the effects of orbital charge-transfer energy and solid–gas contact angle on electrolysis performance. f) The quadratic relationship between orbital charge-transfer energy and intrinsic OER activity in 1 M KOH (sample size $n = 14$, p value < 0.05). The p-value is calculated using one-way ANOVA.

**ADVANCED
SCIENCE NEWS**

www.advancedsciencenews.com

**ADVANCED
MATERIALS**

www.advmat.de

It is worth noting that although the above statistical analysis reveals a positive linear correlation between the charge-transfer energy and performance, the activities actually decrease from $La_{0.5}Sr_{0.5}CoO_{3-x}$ with $\Delta = 0.9$ eV to $LaNiO_{3-x}$ with $\Delta = -0.1$ eV (Figure 4e,f), triggering an issue about the optimal Δ value. To further explore the optimum Δ value, we combined the reported OER activities of $SrCoO_{3-x}$ ($Co^{3.34+}$, $\Delta = 0.64$ eV)[58] and $Zn_{0.5}Co_{0.5}OOH$ ($Co^{3.60+}$, $\Delta = -0.40$ eV)[59] measured under the same conditions for analysis. Corresponding statistical analysis unravels that the relationship between charge-transfer energy (x) and activity (y) is still significant (p value < 0.05) with a quadratic regression equation of $y = 39.092x^2 - 63.693x + 357.492$ (Figure 5f), which means the optimum Δ value is ≈ 1 eV. To further verify the optimum Δ value, we also synthesized and measured other typical perovskite oxides in literatures, namely double perovskite $PrBaCo_2O_{6-x}$ ($Co^{3.23+}$, $\Delta = 1.08$ eV),[12] double perovskite $Gd_{0.5}La_{0.5}BaCo_2O_{6-x}$ ($Co^{3.25+}$, $\Delta = 1.00$ eV),[25] and hexagonal perovskite $Ba_4Sr_4Co_4O_{15-x}$ ($Co^{3.5+}$, $\Delta = 0.00$ eV),[60] as shown in Figures S39 and S40; and Table S1, Supporting Information. We can observe that the new statistical relationships between material charge-transfer energy and their HER/OER performance are still significant under the quadratic regression equations with p values of <0.05, where perovskite oxides with $\Delta \approx 1$ eV exhibit the best HER and OER activities (Figure S40, Supporting Information), corroborating the optimum Δ value (≈ 1 eV).

From the viewpoints of the charge–transfer theory and Sabatier's principle, we can well illustrate this finding. When material Δ is too negative, the excessive mixing of occupied and unoccupied metal 3d–O 2p orbitals at E_F creates unstable O 2p holes[60] (Figure 5f inset), resulting in inferior activities. For the too large Δ values, both occupied and unoccupied orbitals are far away from E_F, leading to the relatively fewer active orbitals and lower orbital electron cloud density around E_F (Figure 5e top) as well as the poor performance. With a neither too large nor too small Δ (≈ 1 eV), catalysts possess the ideal states of active orbitals and orbital electron cloud density for the optimum catalytic activity in line with the Sabatier's principle. This can be attributed to the optimum adsorption/desorption of reactants/intermediates on catalysts with $\Delta \approx 1$ eV, which will be further studied below. Moreover, to evaluate the roles of Δ in the HER/OER performance of 4d/5d-metal-based materials and catalysts with multiple 3d elements, future efforts should be devoted to addressing how to identify the Δ values or establish the possible relationships between other physicochemical properties and Δ for these systems.

2.5. The Unifying Concept for HER Mechanism

Above, we have successfully identified the main universal activity descriptor Δ from material multiple physiochemical properties for HER and OER in different electrolytes. The fine universality, independence, and predictability of Δ will effectively accelerate the rational design of material pristine state to shorten catalyst development periods and lower related costs. To further unravel the underlying roles of Δ in catalysis mechanisms and find or establish a unifying mechanism concept, we combined systematic mechanism experiments, spectral characterizations, and

DFT calculations for our investigations. Both catalysis mechanisms before and after reactions are important due to the fact that the activated active sites and mechanisms after reactions evolve from and strongly rely on material initial states,[34] where we focus on the best-performing and most important Co-based system for study.

Here, we first give insights into the HER active sites and mechanisms before and after the reaction. It has been reported that material transport capacity of the key protons in HER can be reflected by their pH-dependent activities.[61] When material current densities greatly increase with the enlarged pH values of electrolytes, such electrocatalysts exhibit a strong proton transport capacity.[61] With increasing pH values of the solutions, the improvement of the HER current density on $La_{0.5}Sr_{0.5}CoO_{3-x}$ with optimal $\Delta \approx 1$ eV is larger than that on $La_{0.75}Sr_{0.25}CoO_{3-x}$ ($\Delta = 1.5$ eV) and $LaCoO_{3-x}$ ($\Delta = 2$ eV), as shown in Figure S41, Supporting Information; **Figure 6**a. This means that the proton transport capacity of $La_{0.5}Sr_{0.5}CoO_{3-x}$ is the best and the most number of active sites for proton transfer exist in $La_{0.5}Sr_{0.5}CoO_{3-x}$. Tetramethylammonium ions (TMA^+) have been used to cover material surface lattice-oxygen (O^{2-}) sites under the requirement of charge neutrality, which can help understand material active sites.[59,62] To examine material active sites for proton transport in HER, we also measured their HER performance in 1 M tetramethylammonium hydroxide (TMAOH). Compared with the HER current densities in 1 M KOH, the HER activities of three samples in 1 M TMAOH all greatly degrade, especially for $La_{0.5}Sr_{0.5}CoO_{3-x}$ (Figure 6a; Figure S41, Supporting Information), implying the significant role of lattice-oxygen sites for HER. Based on the above XAS study, $La_{0.5}Sr_{0.5}CoO_{3-x}$ with the maximum Co valence ($Co^{3.27+}$) possesses the most lattice-oxygen sites in high-valence Co—O configurations as compared with $La_{0.75}Sr_{0.25}CoO_{3-x}$ ($Co^{3.12+}$) and $LaCoO_{3-x}$ (Co^{3+}) due to the charge balance. Therefore, high-valence Co—O clusters may be the initial active sites for the key proton-transfer steps of HER, which will be further discussed in the unifying mechanism concept and DFT calculations below.

Prior to the analysis of unifying mechanism theory and DFT computations, we need to determine the possible newly formed active compounds or sites on material after HER. Hard XAS and soft XAS spectra before and after HER were measured to study the possible variations of material local structures and electronic structures. Compared to the Co-K XANES spectra before HER, the energy positions at the normalized absorption of 0.8 on Co-K XANES spectra for three samples after HER all shifted to lower energies (Figure 6b), indicating the reduced Co valence. It is noteworthy that the valence reduction after HER for $La_{0.5}Sr_{0.5}CoO_{3-x}$ is larger than that for $La_{0.75}Sr_{0.25}CoO_{3-x}$ and $LaCoO_{3-x}$ (Figure 6b). Considering the reductive nature of HER and reported findings,[31,32] we take the view that parts of the samples are reduced into the Co metal phase. To verify this, we utilized the Co-K extended X-ray absorption fine structure (EXAFS) spectra to investigate the changes in material local structures.[33,47] As shown in Figure 6c, the peak signals at ≈ 1.5 Å, ≈ 2.6 Å, ≈ 3.1 Å, and ≈ 3.4 Å stand for the Co—O shell, multiple scattering contributions, the Co—La/Sr shell, and the corner-shared Co—Co shell, respectively, well with the literatures for this system.[33,63] We can observe that the signal of multiple scattering contributions at ≈ 2.6 Å for all the samples moves

**ADVANCED
SCIENCE NEWS**

www.advancedsciencenews.com

**ADVANCED
MATERIALS**

www.advmat.de
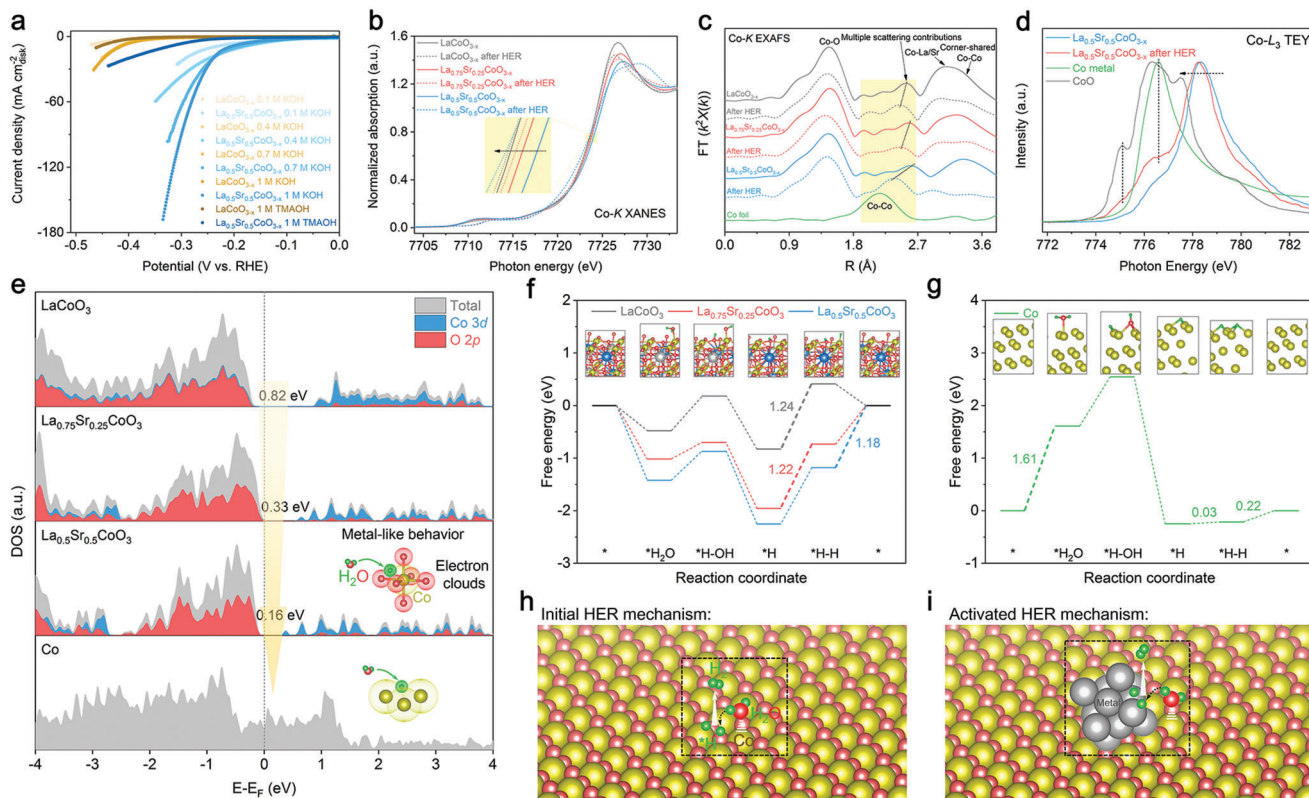
Figure 6. HER mechanism. a) HER activities of $La_{0.5}Sr_{0.5}CoO_{3-x}$ and $LaCoO_{3-x}$ in different electrolytes. b) Co-K XANES and c) corresponding Co-K EXAFS spectra of the Co-based system before and after HER. d) Co-L_3 XAS spectra in TEY mode for pristine $La_{0.5}Sr_{0.5}CoO_{3-x}$, $La_{0.5}Sr_{0.5}CoO_{3-x}$ after HER, Co metal, and CoO reference. e) DOS plots for the Co-based system and Co metal. f,g) Calculated reaction processes on the pristine Co-based system (f) and the formed Co metal after HER (g). h,i) Schematic illustrations of the initial HER mechanism (h) and the activated HER mechanism (i).

toward lower positions, where this shift for $La_{0.5}Sr_{0.5}CoO_{3-x}$ is the largest (yellow transparent box in Figure 6c). By comparing the Co—Co shell at ≈2.2 Å of Co metal (Figure 6c), we prove that this change originates from the partially generated Co metal phase after HER and that the content of formed Co metal phase for $La_{0.5}Sr_{0.5}CoO_{3-x}$ is the highest. The Co-L_3 XAS spectra in TEY mode for $La_{0.5}Sr_{0.5}CoO_{3-x}$ before and after HER further support our conclusion. In comparison to the pristine spectrum, the main peak at Co-L_3 edge of $La_{0.5}Sr_{0.5}CoO_{3-x}$ shifts to lower energy positions after HER (Figure 6d), confirming its reduced Co valence. The reacted $La_{0.5}Sr_{0.5}CoO_{3-x}$ also shows obvious peak signals at ≈776.6 and 775.1 eV, which can be respectively identified as the characteristic signals of Co metal and Co^{2+} ions as compared with corresponding standards in Figure 6d. This demonstrates that the partial Co valence of $La_{0.5}Sr_{0.5}CoO_{3-x}$ reduces to Co^{2+} ions and further to Co metal after HER. Although the electronic structure and local structure of partial materials are changed after reaction, these variations are determined by and evolved from material pristine states, namely the different initial states leading to the different behaviors of $La_{0.5}Sr_{0.5}CoO_{3-x}$, $La_{0.75}Sr_{0.25}CoO_{3-x}$, and $LaCoO_{3-x}$ during HER processes. This is not contradictory with the identification of universal activity descriptors based on material controllable initial states.

Then, based on material pristine structures and the partially generated Co metal phase after HER, we further give insights into the catalysis mechanisms before and after HER via DFT

calculations, aimed at finding or establishing a unifying mechanism concept. Orbital DOS computations were first conducted and compared among $LaCoO_3$, $La_{0.75}Sr_{0.25}CoO_3$, $La_{0.5}Sr_{0.5}CoO_3$, and Co metal. As illustrated in Figure 6e, with increasing Co valence state from $LaCoO_3$ to $La_{0.75}Sr_{0.25}CoO_3$ and further to $La_{0.5}Sr_{0.5}CoO_3$, the whole orbitals shift toward E_F with reduced bandgaps from 0.82 to 0.33 eV and further to 0.16 eV, respectively, approaching to the metallic state of Co metal without bandgap. This accords with the well-known orbital charge-transfer model: with increasing 3d metal valence, the charge-transfer energy Δ decreases accompanied with the shift of orbitals closer to E_F and the reduced bandgap, endowing material with the metal-like feature.[57,64] Material metal-like property has proven to be beneficial for the adsorption of protons,[64,65] which can be ascribed to the facile adsorption of electron-deficient protons on the configurations with metal-like electron flows (Figure 6e inset). To validate this, we performed the detailed calculations for HER steps, following the recognized H_2O adsorption (*H_2O), H_2O dissociation (*H—OH), OH^- desorption (*H), and H_2 formation (*H—H) processes.[28,64,65] As expected, the rate-limiting steps for the initial Co-based system all lie in the function with protons, where the maximum energy barrier reduces from 1.24 eV for $LaCoO_3$ to 1.22 eV for $La_{0.75}Sr_{0.25}CoO_3$ and further to 1.18 eV for $La_{0.5}Sr_{0.5}CoO_3$ (detailed adsorption structures are shown in the inset of Figure 6f). These results corroborate that the metal-like high-valence Co—O clusters in $La_{0.5}Sr_{0.5}CoO_3$ favor proton

adsorption to enhance the HER performance (Figure 6e,f). It is noteworthy that the partially formed Co metal after HER is more favorable for proton adsorption and H_2 releasing (only 0.03 and 0.22 eV, respectively) than metal-like $La_{0.5}Sr_{0.5}CoO_3$ (Figure 6f,g). After HER activation, $La_{0.5}Sr_{0.5}CoO_3$ is still superior to $LaCoO_3$ and $La_{0.75}Sr_{0.25}CoO_3$ because the most Co metal phase is generated on $La_{0.5}Sr_{0.5}CoO_3$ to optimize the steps of proton adsorption and H_2 emission (Figure 6b,c). These findings successfully endow the orbital charge-transfer model as the unifying mechanism concept to demonstrate both mechanisms before and after HER, where the enhanced metal-like property before HER or the partially transformed metal phase after HER promotes the function with the key protons to improve the HER activity (Figure 6e). Noteworthily, the rate-limiting process for the Co metal phase formed after HER is the adsorption of H_2O (1.61 eV in Figure 6g), while this step on the oxygen vacancies of the initial Co-based system is thermodynamically spontaneous (Figure 6f), according well with the literature.[64] Thus, we can well demonstrate the detailed underlying catalysis mechanisms of the model system for HER. Prior to the formation of the Co metal phase, H_2O reactants are adsorbed on material oxygen vacancies; and then, the dissociated protons from adsorbed H_2O transfer to the adjacent metal-like high-valence Co—O active sites for H_2 generation (Figure 6h). After the appearance of the Co metal phase, H_2O molecules still tend to be adsorbed on material oxygen vacancies, while the dissociated protons from adsorbed H_2O now are apt to transfer to the newly-formed Co metal phase with the better proton-adsorption capability for subsequent H_2 production (Figure 6i). Moreover, such mechanism transformation is dynamically stable, which can be supported by the good HER stability of $La_{0.5}Sr_{0.5}CoO_{3-x}$ (Figure S42, Supporting Information). Overall, the key protons for HER tend to be absorbed on the metal-like active sites or phases, following the unifying orbital charge-transfer model.

## 2.6. The Unifying Concept for OER Mechanism

Similarly, we further combined systematic mechanism experiments, spectral characterizations, and first-principle computations to investigate the underlying OER mechanisms and the related unifying mechanism concept.

We first give insights into the possible active sites and catalysis mechanisms of the Co-based system from the mechanism experiments. Currently, the main OER mechanisms include the adsorbate evolution mechanism (AEM) and the lattice oxygen oxidation mechanism (LOM).[29] Through the direct coupling of O—O species from material lattice oxygen sites, the non-acidic LOM pathway can break through the scaling relationships of the AEM processes (i.e., $\Delta G_{*OOH} - \Delta G_{*OH} = 3.2$ eV) to further improve material OER performance, where the participating lattice oxygen sites can be compensated from non-acidic electrolytes.[29,40,47] It has been reported that the LOM pathway can be identified by material pH-dependent OER activities, where the OER current densities of catalyst under LOM processes significantly enhance with increasing pH values of the solutions.[40,47,66] As exhibited in **Figure 7**a; Figure S43, Supporting Information, with increasing electrolytic pH values, all the OER activities of the Co-based system improve, and the improvement for $La_{0.5}Sr_{0.5}CoO_{3-x}$ is

the largest, indicating the most favorable LOM pathway on high-valence $La_{0.5}Sr_{0.5}CoO_{3-x}$ in line with literatures.[29,40,47,66] To verify the important role of lattice-oxygen participation, we also measured the OER performance of the Co-based system in 1 M TMAOH (Figure 7a; Figure S43, Supporting Information). When material lattice-oxygen sites (O^{2-}) are covered by TMA^+ cations under the function of charge neutrality, the OER current densities greatly decline in 1 M TMAOH as compared with those in 1 M KOH, especially for $La_{0.5}Sr_{0.5}CoO_{3-x}$, corroborating the LOM catalysis pathway for $La_{0.5}Sr_{0.5}CoO_{3-x}$. Further, the LOM pathway of the Co-based system is directly demonstrated and compared by the operando ^{18}O isotope labeling measurements.[40,47,66] The degree of material lattice-oxygen participation can be evaluated by comparing the detected intensity of $^{34}O_2$ signals (i.e., $^{16}O^{18}O$) in OER, where the ^{18}O atoms come from the tagged lattice oxygen sites in electrocatalysts.[40,47,66] The detected intensity of $^{34}O_2$ signals enhances from $LaCoO_{3-x}$ to $La_{0.75}Sr_{0.25}CoO_{3-x}$ and further to $La_{0.5}Sr_{0.5}CoO_{3-x}$ (Figure S44, Supporting Information), confirming the more favorable LOM pathway on $La_{0.5}Sr_{0.5}CoO_{3-x}$ than that on $LaCoO_{3-x}$ and $La_{0.75}Sr_{0.25}CoO_{3-x}$. From the standpoint of calculations, the largest energy barrier of LOM pathway on $La_{0.5}Sr_{0.5}CoO_{3-x}$ (0.22 eV) is much lower than that of AEM scenario on $La_{0.5}Sr_{0.5}CoO_{3-x}$ (0.80 eV), as shown in Figure S45, Supporting Information, theoretically corroborating the LOM mechanism on $La_{0.5}Sr_{0.5}CoO_{3-x}$. The beneficial LOM pathway endows $La_{0.5}Sr_{0.5}CoO_{3-x}$ with the optimum OER performance among the Co-based system.

Prior to the identification of a unifying mechanism concept for OER, the possible generated active sites or phases should be figured out after OER. The Co-K XANES, Co-K EXAFS, and Co-L_3 XAS spectra were performed to unravel the underlying changes of material electronic structures and local structures. After the OER oxidation processes, the energy positions at the normalized absorption of 0.8 on the Co-K XANES spectra for the Co-based system after OER all moved to higher energies (Figure 7b), implying their increased Co valence states. It is worth noting that after OER, the Co valence for $La_{0.5}Sr_{0.5}CoO_{3-x}$ was still larger than those for $La_{0.75}Sr_{0.25}CoO_{3-x}$ and $LaCoO_{3-x}$. The multiple scattering contributions at ≈2.6 Å on the Co-K EXAFS spectra for three samples all shifted to lower distances (≈2.4–2.5 Å) after OER (Figure 7c). It has been acknowledged that the appeared signal at ≈2.4–2.5 Å on the Co-K EXAFS spectra after OER can be ascribed to the formation of edge-shared hydroxides.[33,62,67] Combined Co-K XANES and Co-K EXAFS results demonstrate that the Co valence state of partially generated edge-sharing $CoOOH_x$ on $La_{0.5}Sr_{0.5}CoO_{3-x}$ after OER is higher than those on $La_{0.75}Sr_{0.25}CoO_{3-x}$ and $LaCoO_{3-x}$. The formation of high-valence $CoOOH_x$ on $La_{0.5}Sr_{0.5}CoO_{3-x}$ after OER can be further supported by the Co-L_3 XAS spectra in TEY mode. Compared to the pristine Co-L_3 XAS spectrum, the Co-L_3 peak weight of $La_{0.5}Sr_{0.5}CoO_{3-x}$ after OER shifts to higher energy positions and the whole spectral feature becomes narrower (Figure 7d), which are attributed to the generation of the high-valence edge-shared $CoOOH_x$ phase (mixed $Co^{3+/4+}$). The edge-sharing $CoOOH_x$ phase with ≈90° Co—O—Co networks exhibits a weaker inter-site hopping between two Co—O clusters as compared with the initial corner-shared configurations with the Co—O—Co bond angle of ≈180° in ABO_3 structure (Figure S46, Supporting Information),[40] resulting in the narrowed Co-L_3 XAS spectrum after OER (Figure 7d).
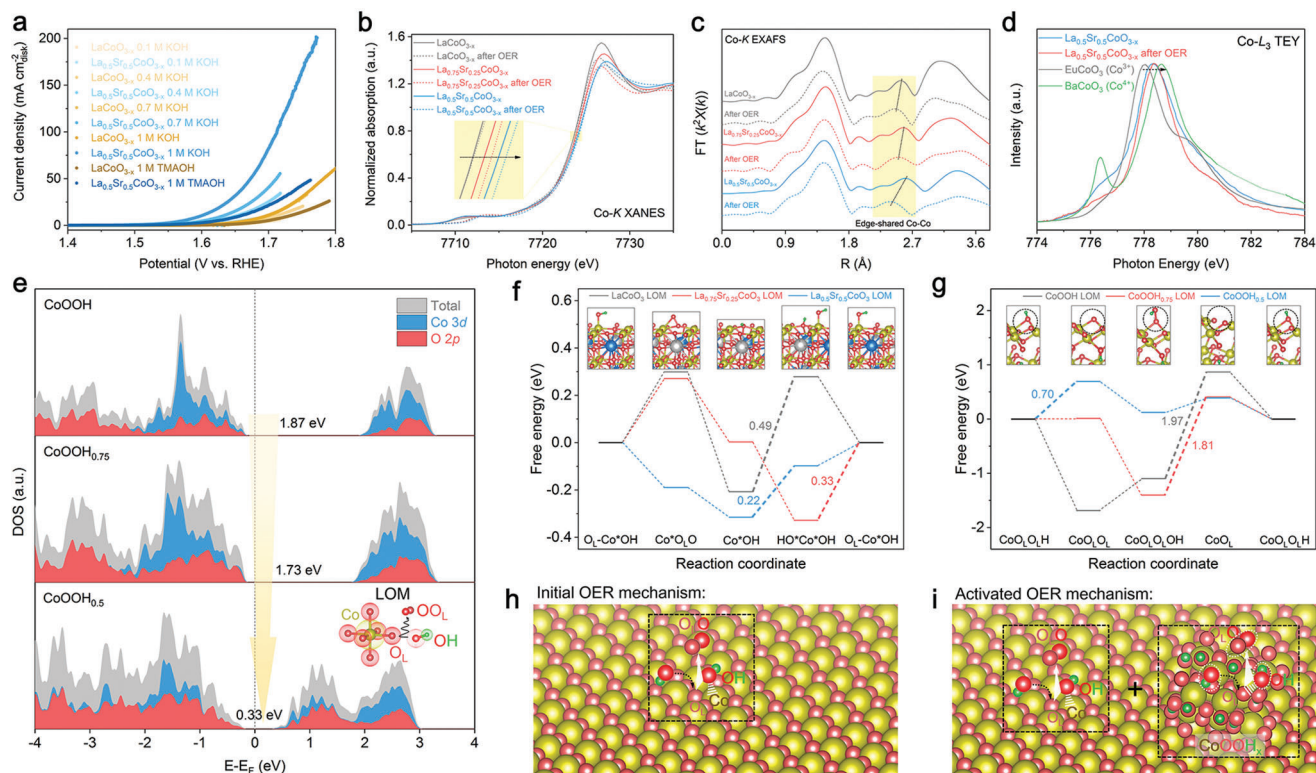
Figure 7. OER mechanism. a) OER activities of $La_{0.5}Sr_{0.5}CoO_{3-x}$ and $LaCoO_{3-x}$ in different electrolytes. b) The Co-K XANES and c) corresponding Co-K EXAFS spectra of the Co-based system before and after OER. d) The Co-L_3 XAS spectra in TEY mode for pristine $La_{0.5}Sr_{0.5}CoO_{3-x}$, $La_{0.5}Sr_{0.5}CoO_{3-x}$, after OER, $EuCoO_3$ (pure Co^{3+}), and $BaCoO_3$ (pure Co^{4+}) reference. e) The DOS plots for $CoOOH$, $CoOOH_{0.75}$, and $CoOOH_{0.5}$. f,g) Calculated LOM processes on the pristine Co-based system (f) and the formed $CoOOH_x$ phases after OER (g). h,i) Schematic illustrations of the initial OER mechanism (h) and the activated OER mechanism (i).

Based on the pristine structure before OER and the $CoOOH_x$ phase that formed after OER, we conducted systematic theoretical calculations and attempted to find a unifying mechanism concept for OER. To reveal the electronic structure of the $CoOOH_x$ phase after OER, we first calculated the DOS for $CoOOH$ (Co^{3+}), $CoOOH_{0.75}$ ($Co^{3.25+}$), and $CoOOH_{0.5}$ ($Co^{3.5+}$). With increasing Co valence from $CoOOH$ (Co^{3+}) to $CoOOH_{0.75}$ ($Co^{3.25+}$) and further to $CoOOH_{0.5}$ ($Co^{3.5+}$), the whole orbitals move towards E_F and the related bandgap reduces from 1.87 to 1.73 eV and further to 0.33 eV (Figure 7e), respectively, contributing to the enhanced orbital electron cloud density around E_F. These findings can also be rationalized by the orbital charge-transfer model: the charge-transfer energy reduces with the increase in the valence of 3d element, accompanied with the shift of orbitals closer to E_F and the enhanced orbital electron cloud density around E_F (particularly for the O 2p orbital) to trigger the beneficial LOM pathway[57,66] (Figure 5e top and Figure 7e inset). To further examine the universality of the orbital charge-transfer model, we calculated the detailed LOM processes on pristine structures and the generated $CoOOH_x$ phases after OER. As expected in Figure 7f, prior to the formation of $CoOOH_x$ phase, pristine $La_{0.5}Sr_{0.5}CoO_3$ with the highest Co valence shows the lowest maximum energy barrier (0.22 eV) in the LOM pathway as compared with relatively low-valence $La_{0.75}Sr_{0.25}CoO_3$ (0.33 eV) and $LaCoO_3$ (0.49 eV). Similarly, after the generation of $CoOOH_x$ phase, the maximum energy barrier in LOM processes reduces

from 1.97 eV for $CoOOH$ to 1.81 eV for $CoOOH_{0.75}$ and further to 0.70 eV for $CoOOH_{0.5}$ (Figure 7g). These verify the more favorable LOM pathway on the relatively high-valence materials with high O 2p orbital electron cloud density around E_F, following the unifying orbital charge-transfer theory. It is noteworthy that the whole maximum energy barriers in LOM for edge-sharing $CoOOH_x$ phases after OER are larger than those for initial corner-sharing ABO_3 structures because of their different inter-site hopping effects[40] as discussed above (Figure S46, Supporting Information). This means that the catalysis mechanism is a coupled LOM process on both pristine corner-sharing ABO_3 and formed edge-sharing $CoOOH_x$ phases after OER. Specifically, the initial LOM pathway tends to occur on the lattice-oxygen sites of pristine high-valence Co—O clusters (Figure 7h), while the activated coupled LOM processes take place in the lattice-oxygen sites of high-valence Co—O configurations in both the initial corner-sharing ABO_3 structures and the edge-sharing $CoOOH_x$ phases after OER (Figure 7i), following the unifying orbital charge-transfer model. In addition, material participated lattice-oxygen sites in non-acidic LOM can be continuously compensated from OH^- containing electrolytes[29,40,47] (Figure 7h,i), contributing to the dynamically stable catalysis processes and the fine OER stability of $La_{0.5}Sr_{0.5}CoO_{3-x}$ (Figure S47, Supporting Information).

Till now, we have successfully identified the orbital charge-transfer model as the unifying mechanism concept for "green

**ADVANCED
SCIENCE NEWS**

www.advancedsciencenews.com

**ADVANCED
MATERIALS**

www.advmat.de
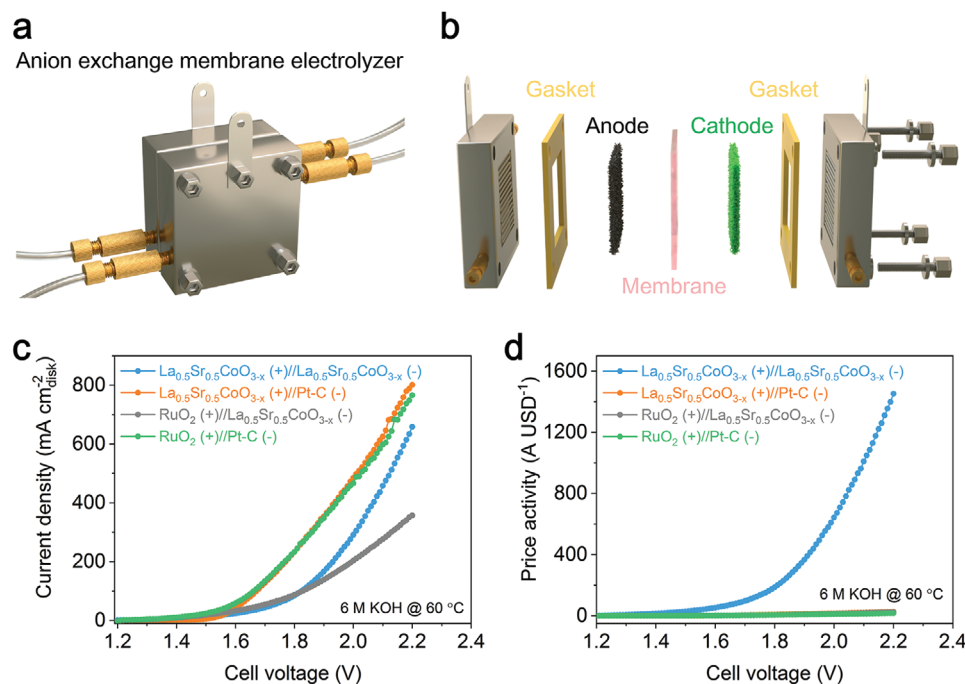
Figure 8. AEME application. a,b) Schematic diagrams of the whole assembled AEME cell (a) and the detailed components in the AEME cell (b). c) The cell performance and the d) price activity of different combinations by using $La_{0.5}Sr_{0.5}CoO_{3-x}$ and noble-metal-based benchmarks as anode or cathode in 6 M KOH under 60 °C.

hydrogen" production, which can be applied as a powerful mechanism analysis tool and foundation.

2.7. AEME Application

In addition to finding a universal activity descriptor and a unifying mechanism concept for "green hydrogen" production, a practical AEME application in the lab scale[68] was further constructed to compare the performance of the optimum $La_{0.5}Sr_{0.5}CoO_{3-x}$ in our model system with the state-of-the-art noble-metal-based benchmarks. As presented in **Figure 8**a,b, the AEME cell is composed of current collectors, gaskets, anode, cathode, and membrane, where the electrolyte is in flow mode. Electrocatalysts were prepared with the same loading on the Ni foam to serve as the anode or cathode. To move a step closer to the industrial conditions,[8] all the AEME measurements were performed in 6 M KOH under 60 °C. The state-of-the-art precious-metal-based benchmarks of RuO_2 for OER and Pt/C for HER were chosen for comparison. As shown in Figure 8c, the onset voltages of the AEME cell with $La_{0.5}Sr_{0.5}CoO_{3-x}$ as anode or cathode were comparable to the combination with RuO_2 as anode and Pt/C as cathode. Noteworthily, the couple with $La_{0.5}Sr_{0.5}CoO_{3-x}$ as an anode and Pt/C as a cathode was even slightly superior to the combination of RuO_2 and Pt/C (Figure 8c), demonstrating the remarkable OER activity of $La_{0.5}Sr_{0.5}CoO_{3-x}$. Future efforts should be devoted to further improving the HER performance of non-noble-metal-based oxides. Considering that cost is an important criterion in the practical application, we further compared the price activity normalized to material respective cost. Impressively, the bifunctional couple using $La_{0.5}Sr_{0.5}CoO_{3-x}$ as both anode and cathode

exhibits much better price activity than the other combinations containing noble-metal-based benchmarks (Figure 8d). In addition, the bi-functional combination of our oxide shows a fine stability (Figure S48, Supporting Information). These endow our nonprecious-metal-based oxide with a high competitive potential in the future commercial applications for "green hydrogen" production.

3. Conclusion

We have successfully solved two pivotal scientific issues in the designing and screening of efficient electrocatalysts for "green hydrogen" production. First, through the powerful statistical analysis, the main universal activity descriptor (orbital charge-transfer energy) has been rationally extracted from 13 representative material properties of 12 3d-metal-based model oxides. Its high relevance with activity, good independence from other parameters, and fine predictability in the design of material pristine state enable to rationalize and guide both HER and OER performance in 1 M KOH, 1 M KPi, and 6 M KOH, which will help avoid time-consuming and high-cost trials and errors in fundamental research and commercialization. Second, combined systematic mechanism experiments, spectral characterizations, and first-principle computations have successfully identified that the orbital charge-transfer theory can serve as the unifying concept to demonstrate the life-cycle HER and OER catalysis mechanisms, offering a powerful mechanism analysis tool and foundation. We believe our findings will provide critical guidance for rational material design and mechanism understanding in many potential fields.

4. Experimental Section

Material Synthesis: All the $La_ySr_{1-y}MO_{3-x}$ (M = pure Mn, Fe, Co, or Ni; y = 1, 0.75, and 0.5) perovskite oxides were prepared by the sol–gel method.[25,47] Stoichiometric amounts of the respective metal nitrates (analytical grade) were dissolved in the deionized water, followed by the complexation with citric acid (CA) and ethylenediaminetetraacetic acid (EDTA). The mole ratio of CA vs EDTA vs total metal ions was 2:1:1. The pH value of the mixed solutions was controlled at 6–7 by adding the NH_3 aqueous solution. A transparent gel was achieved by heating the mixed solutions under ≈90° with continuous stirring. The gel was then heated under ≈250 °C for 10 h to obtain the solid precursor. The oxide powders were finally acquired by calcinating the solid precursors under 1000 °C for 5 h. The commercial Pt/C (50 wt% Pt) and RuO_2 benchmarks were purchased from Alfa Alsar and Sigma–Aldrich, respectively.

Characterizations: The XRD results were collected on an X-ray diffractometer with filtered Cu-Kα radiation at a wavelength of 1.5418 Å. The XRD refinement was conducted through the TOPAS software. Material BET value and room-temperature electrical conductivity were acquired on Quantachrome Autosorb-iQ$_3$ equipment and a four-probe direct-current instrument with the Keithley 2420 source meter, respectively. The 3d-K hard XAS spectra and 3d-L/O-K soft XAS results (in TEY mode) were performed at TPS 44A and TLS 20A of the NSRRC in Taiwan, respectively, where respective standards were simultaneously measured for the energy calibration. The 3d-K XANES and EXAFS data were analyzed via the ATHENA software packages.

Statistical Analysis: Regression analysis is a statistical technique that characterizes the functional relationship between dependent and predictor variables. Linear regression illustrates the relationship between a dependent variable and one or more predictor variables using a linear equation. The linear regression is represented by the equation: $Y = a_0 + a_1X_1 + a_2X_2 + \cdots + a_nX_n$, where Y is the dependent variable; X_1, X_2, and X_n are the predictor variables; and a_0, a_1, a_2, and a_n are the regression coefficients. The equation for quadratic regression can be expressed as $Y = a_0 + a_1X + a_2X^2$. Logarithmic regression is very useful for modeling data that initially increases or declines swiftly and then gradually. The natural logarithmic function is formulated as $Y = a_0 + a_1\ln X$. The natural exponential function is the inverse of the natural logarithmic function with the form of $Y = a_0e^{a_1X}$. In this study, regression analysis was performed using IBM SPSS Statistics 25.0 software.

Electrochemical Measurements: The electrochemical measurements on glassy carbon electrodes (GCE) in different electrolytes at 25 °C were carried out on an SP-300 workstation (Bio-Logic) with a standard three-electrode configuration, where the GCE (0.196 cm^{-2}, Pine Research Instrumentation), reversible hydrogen electrode (RHE, Phychemi Company Limited), and graphite rod served as the working, reference and counter electrodes, respectively. The working electrodes were prepared by the catalyst ink under a loading of 0.232 mg cm^{-2}_{disk}, where the homogeneous catalyst ink was obtained by dispersing 10 mg oxide powder, 10 mg carbon black, and 0.1 mL 5 wt% Nafion solution in 1.0 mL absolute ethanol after sonication. All the electrochemical measurements on GCE were conducted in Ar-saturated (for HER) or O_2-saturated (for OER) electrolytes at the rotating speeds of 2400 rpm for HER and 1600 rpm for OER. The catalyst loading for the stability measurements on carbon paper was 2 mg cm^{-2}_{disk}. The AEME measurements were performed in 6 M KOH at 60 °C with a catalyst loading of 2 mg cm^{-2}_{disk}. The AEME membrane was bought from the Fuel Cell Store (Pention-AEM-72-05) with a thickness of 50 μm.

The ^{18}O-Isotope-Labeling Method: The catalysts were prepared on the carbon paper with a loading of 1 mg cm^{-2}_{disk} and activated at 10 mA cm^{-2}_{disk} for 30 min in 1 M KOH with the ^{18}O isotope to anchor the ^{18}O atoms into material lattice. Then, electrode surface dissociative ^{18}O atoms were washed away by fresh 1 M KOH without the ^{18}O isotope. The ^{18}O-labeled samples were measured for two OER cycles in the fresh 1 M KOH without the ^{18}O isotope in the H-type cell using Ar as the carrier gas. The online electrochemical mass spectroscopy (ThermoStar, Pfeiffer Vacuum) was connected with the well-sealed H-type cell to analyze the gas signals. The final $^{34}O_2$ signals were subtracted by the contributions of the natural ^{18}O isotope in water (≈0.2%) to reveal the real material lattice-oxygen participation in OER.[66] The ^{18}O isotope was purchased from Taiyo Nippon Sanso (≥98 atom% ^{18}O).

First-Principle Computations: All spin-polarized DFT computations were conducted through the Vienna Ab initio Simulation Package (VASP)[69] with the projector-augmented wave (PAW) method.[70] The generalized gradient approximation (GGA) formulated by the Perdew–Burke–Ernzerhof (PBE) was applied to describe the exchange-correlation function. The effective U values of 4.0 eV for Mn-based oxides, 5.3 eV for Fe-based oxides, 3.5 eV for Co-based oxides, and 6.4 eV for Ni-based oxides were used under the Hubbard U model (DFT + U).[40,43,71] The van der Waals (vdW) interactions and the interactions between the atomic core and electrons were described by the DFT-D3 method in Grimme's scheme[72] and the PAW method, respectively. The plane-wave basis-set energy cutoff was 500 eV. The Brillouin zone was sampled with Gamma (Γ)-centered Monkhorst–Pack mesh sampling (3 × 3 × 1 for all surface structures and at least 5 × 5 × 5 for all bulk structures) for geometry relaxation. To ensure negligible lateral interaction of adsorbates, a vacuum spacing of ≈15 Å was introduced for all the slabbed models. About half of the bottom layers were kept frozen in the lattice position. All structures with a dynamic magnetic moment were fully relaxed and optimized until their average residual forces and total energies were <0.02 eV $Å^{-1}$ and $<1 \times 10^{-6}$ eV, respectively. The Gibbs free energy calculations were operated with the computational hydrogen electrode (CHE) model.[73,74]

Supporting Information

Supporting Information is available from the Wiley Online Library or from the author.

Acknowledgements

Conflict of Interest

The authors declare no conflict of interest.

Author Contributions

D.G., H.X., Q.Z., and Y.-C.H. contributed equally to this work. D.G. and Z.S. proposed, designed, and funded this work. Z.H. and M.N. gave helpful suggestions to improve the study. D.G. and C.S. carried out the synthesis, laboratory characterizations, and electrochemical measurements. H.X. performed all the DFT calculations. Q.Z. conducted all the statistical analysis. Y.-C.H., Y.-C.C., C.-W.P., S.-C.H., J.-M.C., and Z.H. measured the soft and hard XAS spectra. X.X. carried out the ^{18}O-isotope-labeling experiments. J.T. performed the AEME measurements. Y.G. was involved in some laboratory characterizations. D.G. analyzed all the data and discussed the results with other coauthors. D.G. wrote the manuscript and all the authors edited it.

Data Availability Statement

The data that support the findings of this study are available from the corresponding author upon reasonable request.

[1] G. M. Whitesides, G. W. Crabtree, *Science* **2007**, *315*, 796.

[2] *Net Zero by 2050: A Roadmap for the Global Energy Sector*, International Energy Agency, **2021**.

[3] *Global Hydrogen Review 2021*, International Energy Agency, **2021**.

[4] *Hydrogen for Net-Zero: A Critical Cost-Competitive Energy Vector*, Hydrogen Council and McKinsey & Company, **2021**.

[5] *Hydrogen insights: a perspective on hydrogen investment, market development and cost competitiveness*, Hydrogen Council and McKinsey & Company, **2021**.

[6] T. Braun, K. Baert, *Coal vs Methane vs Water: The Future of Hydrogen Production*, Kawasaki Heavy Industries, **2022**.

[7] A. R. Smith, J. Klosek, *Fuel Process. Technol.* **2001**, *70*, 115.

[8] *Green Hydrogen Cost Reduction: Scaling Up Electrolysers to Meet the 1.5 °C Climate Goal*, International Renewable Energy Agency, **2020**.

[9] Z. W. Seh, J. Kibsgaard, C. F. Dickens, I. Chorkendorff, J. K. Nørskov, T. F. Jaramillo, *Science* **2017**, *355*, eaad4998.

[10] I. C. Man, H.-Y. Su, F. Calle-Vallejo, H. A. Hansen, J. I. Martínez, N. G. Inoglu, J. Kitchin, T. F. Jaramillo, J. K. Nørskov, J. Rossmeisl, *ChemCatChem* **2011**, *3*, 1159.

[11] J. Suntivich, K. J. May, H. A. Gasteiger, J. B. Goodenough, Y. Shao-Horn, *Science* **2011**, *334*, 1383.

[12] A. Grimaud, K. J. May, C. E. Carlton, Y. L. Lee, M. Risch, W. T. Hong, J. Zhou, Y. Shao-Horn, *Nat. Commun.* **2013**, *4*, 2439.

[13] W. T. Hong, K. A. Stoerzinger, Y.-L. Lee, L. Giordano, A. Grimaud, A. M. Johnson, J. Hwang, E. J. Crumlin, W. Yang, Y. Shao-Horn, *Energy Environ. Sci.* **2017**, *10*, 2190.

[14] F. Calle-Vallejo, N. G. Inoglu, H.-Y. Su, J. I. Martínez, I. C. Man, M. T. M. Koper, J. R. Kitchin, J. Rossmeisl, *Chem. Sci.* **2013**, *4*, 1245.

[15] D. Wu, C. Dong, H. Zhan, X. W. Du, *J. Phys. Chem. Lett.* **2018**, *9*, 3387.

[16] J. O. M. Bockris, T. Otagawa, *J. Electrochem. Soc.* **1984**, *131*, 290.

[17] F. Calle-Vallejo, O. A. Díaz-Morales, M. J. Kolb, M. T. M. Koper, *ACS Catal.* **2015**, *5*, 869.

[18] S. Trasatti, *J. Electroanal. Chem.* **1980**, *111*, 125.

[19] X. Li, Y. Bai, Z. Cheng, *Adv. Sci.* **2021**, *8*, 2101000.

[20] D. A. Kuznetsov, B. Han, Y. Yu, R. R. Rao, J. Hwang, Y. Román-Leshkov, Y. Shao-Horn, *Joule* **2018**, *2*, 225.

[21] N. Govindarajan, J. M. García-Lastra, E. J. Meijer, F. Calle-Vallejo, *Curr. Opin. Electrochem.* **2018**, *8*, 110.

[22] J. Greeley, T. F. Jaramillo, J. Bonde, I. B. Chorkendorff, J. K. Nørskov, *Nat. Mater.* **2006**, *5*, 909.

[23] B. Hammer, J. K. Nørskov, *Nature* **1995**, *376*, 238.

[24] D. Cao, H. Xu, H. Li, C. Feng, J. Zeng, D. Cheng, *Nat. Commun.* **2022**, *13*, 5843.

[25] D. Guan, J. Zhou, Y. C. Huang, C. L. Dong, J. Q. Wang, W. Zhou, Z. Shao, *Nat. Commun.* **2019**, *10*, 3755.

[26] T. He, W. Wang, F. Shi, X. Yang, X. Li, J. Wu, Y. Yin, M. Jin, *Nature* **2021**, *598*, 76.

[27] Y. Dou, Y. Xie, X. Hao, T. Xia, Q. Li, J. Wang, L. Huo, H. Zhao, *Appl. Catal., B* **2021**, *297*, 120403.

[28] Y. Jiao, Y. Zheng, M. Jaroniec, S. Z. Qiao, *Chem. Soc. Rev.* **2015**, *44*, 2060.

[29] J. Song, C. Wei, Z. F. Huang, C. Liu, L. Zeng, X. Wang, Z. J. Xu, *Chem. Soc. Rev.* **2020**, *49*, 2196.

[30] H. Jiang, Q. He, Y. Zhang, L. Song, *Acc. Chem. Res.* **2018**, *51*, 2968.

[31] Y. Zhu, H.-C. Chen, C.-S. Hsu, T.-S. Lin, C.-J. Chang, S.-C. Chang, L.-D. Tsai, H. M. Chen, *ACS Energy Lett.* **2019**, *4*, 987.

[32] C. Hu, Q. Ma, S.-F. Hung, Z.-N. Chen, D. Ou, B. Ren, H. M. Chen, G. Fu, N. Zheng, *Chem* **2017**, *3*, 122.

[33] M. Risch, A. Grimaud, K. J. May, K. A. Stoerzinger, T. J. Chen, A. N. Mansour, Y. Shao-Horn, *J. Phys. Chem. C* **2013**, *117*, 8628.

[34] D. Guan, W. Zhou, Z. Shao, *Small Sci.* **2021**, *1*, 2100030.

[35] J. Hwang, R. R. Rao, L. Giordano, Y. Katayama, Y. Yu, Y. Shao-Horn, *Science* **2017**, *358*, 751.

[36] W. Yin, B. Weng, J. Ge, Q. Sun, Z. Li, Y. Yan, *Energy Environ. Sci.* **2019**, *12*, 442.

[37] L. Held, M. Ott, *Annu. Rev. Stat. Appl.* **2018**, *5*, 393.

[38] N. Fumo, M. A. R. Biswas, *Renewable Sustainable Energy Rev.* **2015**, *47*, 332.

[39] G. Liu, W. S. Y. Wong, M. Kraft, J. W. Ager, D. Vollmer, R. Xu, *Chem. Soc. Rev.* **2021**, *50*, 10674.

[40] H. Zhang, Y. Gao, H. Xu, D. Guan, Z. Hu, C. Jing, Y. Sha, Y. Gu, Y. C. Huang, Y. C. Chang, C. W. Pao, X. Xu, J. F. Lee, Y. Y. Chin, H. J. Lin, C. T. Chen, Y. Chen, Y. Guo, M. Ni, W. Zhou, Z. Shao, *Adv. Funct. Mater.* **2022**, *32*, 2207618.

[41] X. Xu, Y. Chen, W. Zhou, Z. Zhu, C. Su, M. Liu, Z. Shao, *Adv. Mater.* **2016**, *28*, 6442.

[42] A. Khorsand Zak, W. H. Abd. Majid, M. E. Abrishami, R. Yousefi, *Solid State Sci.* **2011**, *13*, 251.

[43] D. Guan, J. Zhong, H. Xu, Y.-C. Huang, Z. Hu, B. Chen, Y. Zhang, M. Ni, X. Xu, W. Zhou, Z. Shao, *Appl. Phys. Rev.* **2022**, *9*, 011422.

[44] S. Agrestini, K. Chen, C. Y. Kuo, L. Zhao, H. J. Lin, C. T. Chen, A. Rogalev, P. Ohresser, T. S. Chan, S. C. Weng, G. Auffermann, A. Völzke, A. C. Komarek, K. Yamaura, M. W. Haverkort, Z. Hu, L. H. Tjeng, *Phys. Rev. B* **2019**, *100*, 014443.

[45] J. Yang, L. Zhou, J. Cheng, Z. Hu, C. Kuo, C. W. Pao, L. Jang, J. F. Lee, J. Dai, S. Zhang, S. Feng, P. Kong, Z. Yuan, J. Yuan, Y. Uwatoko, T. Liu, C. Jin, Y. Long, *Inorg. Chem.* **2015**, *54*, 6433.

[46] Z. Zeng, M. Greenblatt, M. A. Subramanian, M. Croft, *Phys. Rev. Lett.* **1999**, *82*, 3164.

[47] D. Guan, K. Zhang, Z. Hu, X. Wu, J. L. Chen, C. W. Pao, Y. Guo, W. Zhou, Z. Shao, *Adv. Mater.* **2021**, *33*, 2103392.

[48] A. Juhin, F. de Groot, G. Vankó, M. Calandra, C. Brouder, *Phys. Rev. B* **2010**, *81*, 115115.

[49] N. Hollmann, Z. Hu, M. Valldor, A. Maignan, A. Tanaka, H. H. Hsieh, H. J. Lin, C. T. Chen, L. H. Tjeng, *Phys. Rev. B* **2009**, *80*, 085111.

[50] S. Nemrava, D. A. Vinnik, Z. Hu, M. Valldor, C. Y. Kuo, D. A. Zherebtsov, S. A. Gudkova, C. T. Chen, L. H. Tjeng, R. Niewa, *Inorg. Chem.* **2017**, *56*, 3861.

[51] H. Guo, Z. W. Li, L. Zhao, Z. Hu, C. F. Chang, C. Y. Kuo, W. Schmidt, A. Piovano, T. W. Pi, O. Sobolev, D. I. Khomskii, L. H. Tjeng, A. C. Komarek, *Nat. Commun.* **2018**, *9*, 43.

[52] A. Fujimori, A. E. Bocquet, T. Saitoh, T. Mizokawa, *J. Electron Spectrosc. Relat. Phenom.* **1993**, *62*, 141.

[53] A. E. Bocquet, T. Mizokawa, T. Saitoh, H. Namatame, A. Fujimori, *Phys. Rev. B* **1992**, *46*, 3771.

[54] I. Yamada, A. Takatsu, K. Asai, T. Shirakawa, H. Ohzuku, A. Seno, T. Uchimura, H. Fujii, S. Kawaguchi, K. Wada, H. Ikeno, S. Yagi, *J. Phys. Chem. C* **2018**, *122*, 27885.

[55] C. F. Chang, T. C. Koethe, Z. Hu, J. Weinen, S. Agrestini, L. Zhao, J. Gegner, H. Ott, G. Panaccione, H. Wu, M. W. Haverkort, H. Roth, A. C. Komarek, F. Offi, G. Monaco, Y. F. Liao, K. D. Tsuei, H. J. Lin, C. T. Chen, A. Tanaka, L. H. Tjeng, *Phys. Rev. X* **2018**, *8*, 021004.

[56] D. Edelmann, T. F. Móri, G. J. Székely, *Stat. Probab. Lett.* **2021**, *169*, 108960.

**ADVANCED
SCIENCE NEWS**

www.advancedsciencenews.com

**ADVANCED
MATERIALS**

www.advmat.de

[57] D. Guan, K. Zhang, W. Zhou, Z. Shao, *Curr. Opin. Electrochem.* **2021**, *30*, 100805.

[58] Y. Pan, X. Xu, Y. Zhong, L. Ge, Y. Chen, J. M. Veder, D. Guan, R. O'Hayre, M. Li, G. Wang, H. Wang, W. Zhou, Z. Shao, *Nat. Commun.* **2020**, *11*, 2002.

[59] Z.-F. Huang, J. Song, Y. Du, S. Xi, S. Dou, J. M. V. Nsanzimana, C. Wang, Z. J. Xu, X. Wang, *Nat. Energy* **2019**, *4*, 329.

[60] Y. Zhu, H. A. Tahini, Z. Hu, Z. G. Chen, W. Zhou, A. C. Komarek, Q. Lin, H. J. Lin, C. T. Chen, Y. Zhong, M. T. Fernandez-Diaz, S. C. Smith, H. Wang, M. Liu, Z. Shao, *Adv. Mater.* **2020**, *32*, 1905025.

[61] C. Yang, C. Laberty-Robert, D. Batuk, G. Cibin, A. V. Chadwick, V. Pimenta, W. Yin, L. Zhang, J. M. Tarascon, A. Grimaud, *J. Phys. Chem. Lett.* **2017**, *8*, 3466.

[62] D. Guan, C. Shi, H. Xu, Y. Gu, J. Zhong, Y. Sha, Z. Hu, M. Ni, Z. Shao, *J Energy Chem* **2023**, *82*, 572.

[63] S. K. Pandey, S. Khalid, N. P. Lalla, A. V. Pimpale, *J. Phys.: Condens. Matter* **2006**, *18*, 10617.

[64] D. Guan, J. Zhou, Z. Hu, W. Zhou, X. Xu, Y. Zhong, B. Liu, Y. Chen, M. Xu, H. J. Lin, C. T. Chen, J. Wang, Z. Shao, *Adv. Funct. Mater.* **2019**, *29*, 1900704.

[65] M. Gong, W. Zhou, M. C. Tsai, J. Zhou, M. Guan, M. C. Lin, B. Zhang, Y. Hu, D. Y. Wang, J. Yang, S. J. Pennycook, B. J. Hwang, H. Dai, *Nat. Commun.* **2014**, *5*, 4695.

[66] A. Grimaud, O. Diaz-Morales, B. Han, W. T. Hong, Y. L. Lee, L. Giordano, K. A. Stoerzinger, M. T. M. Koper, Y. Shao-Horn, *Nat. Chem.* **2017**, *9*, 457.

[67] D. Guan, G. Ryu, Z. Hu, J. Zhou, C.-L. Dong, Y.-C. Huang, K. Zhang, Y. Zhong, A. C. Komarek, M. Zhu, X. Wu, C.-W. Pao, C.-K. Chang, H.-J. Lin, C.-T. Chen, W. Zhou, Z. Shao, *Nat. Commun.* **2020**, *11*, 3376.

[68] J. Tang, X. Xu, T. Tang, Y. Zhong, Z. Shao, *Small Methods* **2022**, *6*, 2201099.

[69] G. Kresse, J. Furthmüller, *Phys. Rev. B* **1996**, *54*, 11169.

[70] P. E. Blöchl, *Phys. Rev. B* **1994**, *50*, 17953.

[71] Y. Sun, H. Liao, J. Wang, B. Chen, S. Sun, S. J. H. Ong, S. Xi, C. Diao, Y. Du, J.-O. Wang, M. B. H. Breese, S. Li, H. Zhang, Z. J. Xu, *Nat. Catal.* **2020**, *3*, 554.

[72] S. Grimme, J. Antony, S. Ehrlich, H. Krieg, *J. Chem. Phys.* **2010**, *132*, 154104.

[73] A. A. Peterson, F. Abild-Pedersen, F. Studt, J. Rossmeisl, J. K. Nørskov, *Energy Environ. Sci.* **2010**, *3*, 1311.

[74] H. Xu, D. Guan, L. Ma, *Nanoscale* **2023**, *15*, 2756.